

# Low-luminosity X-ray sources and the Galactic ridge X-ray emission

R. S. Warwick<sup>1\*</sup>

<sup>1</sup>*Department of Physics and Astronomy, University of Leicester, University Road, Leicester, LE1 7RH, UK*

Accepted. Received; in original form

## ABSTRACT

Using the *XMM-Newton* Slew Survey, we construct a hard-band selected sample of low-luminosity Galactic X-ray sources. Two source populations are represented, namely coronally-active stars and binaries (ASBs) and cataclysmic variables (CVs), with X-ray luminosities collectively spanning the range  $10^{28-34}$  erg s<sup>−1</sup> (2–10 keV). We derive the 2–10 keV X-ray luminosity function (XLF) and volume emissivity of each population. Scaled to the local stellar mass density, the latter is found to be  $1.08 \pm 0.16 \times 10^{28}$  erg s<sup>−1</sup> M<sub>⊙</sub><sup>−1</sup> and  $2.5 \pm 0.6 \times 10^{27}$  erg s<sup>−1</sup> M<sub>⊙</sub><sup>−1</sup>, for the ASBs and CVs respectively, which in total is a factor 2 higher than previous estimates. We employ the new XLFs to predict the X-ray source counts on the Galactic plane at  $l = 28.5^\circ$  and show that the result is consistent with current observational constraints. The X-ray emission of faint, unresolved ASBs and CVs can account for a substantial fraction of the Galactic ridge X-ray emission (GRXE). We discuss a model in which  $\sim 80$  per cent of the 6–10 keV GRXE intensity is produced in this way, with the remainder attributable to X-ray scattering in the interstellar medium and/or young Galactic source populations. Much of the hard X-ray emission attributed to the ASBs is likely to be produced during flaring episodes.

**Key words:** stars: dwarf novae - novae, cataclysmic variables - X-rays: binaries - X-rays: stars

## 1 INTRODUCTION

The hard Galactic ridge X-ray emission (GRXE) can be traced from the Galactic Centre, where its surface brightness peaks, along the Galactic plane out to  $|l| = 60^\circ$  and beyond (Worrall et al. 1982; Warwick et al. 1985; Koyama et al. 1986a; Yamauchi & Koyama 1993; Yamauchi et al. 1996; Revnivtsev et al. 2006; Koyama et al. 2007). In the 4–10 keV band the spectrum of the GRXE resembles that of 5–10 keV optically-thin thermal plasma in collisional ionization equilibrium, with prominent lines arising from K-shell emission in He-like and H-like Fe at 6.67 keV and 6.96 keV, respectively (Koyama et al. 1986a; Kaneda et al. 1997). An Fe K $\alpha$  line at 6.4 keV resulting from the fluorescence of neutral or near-neutral Fe is also seen (Koyama et al. 1996; Ebisawa et al. 2008; Yamauchi et al. 2009). Below 4 keV, emission lines of abundant elements such as Mg, Si, S, Ar and Ca are evident, with the He-like to H-like intensity ratios (taken together with those of Fe) indicative of a multi-temperature plasma (Kaneda et al. 1997; Tanaka 2002). The temperature structure appears to be similar at different locations along the GRXE, with the exception of the region within a degree or so of the Galactic Centre (Uchiyama et al. 2011, 2013). Above 10 keV the GRXE spectrum may exhibit a hard powerlaw tail, possibly extending to the hard X-ray/ $\gamma$ -ray re-

gion (Yamasaki et al. 1997; Valinia & Marshall 1998; Strong et al. 2005; Krivonos et al. 2007).

The GRXE has been interpreted both in terms of the superposition of faint point sources (Sugizaki et al. 2001; Revnivtsev et al. 2006; Yuasa et al. 2012) and as a highly energetic, very high temperature phase of the interstellar medium (Koyama et al. 1986b; Kaneda et al. 1997; Tanaka 2002), amongst other possibilities (e.g. Valinia et al. 2000; Molaro et al. 2014). Recent studies have shown that the GRXE surface brightness follows that of the near infra-red (NIR) light associated with the old stellar population of the Galaxy (Revnivtsev et al. 2006). Also very deep *Chandra* observations have directly resolved over 80% of the GRXE near the Galactic Centre into point sources (Revnivtsev et al. 2009; Hong 2012). This is compelling evidence that the bulk of GRXE originates in the integrated emission of point sources, although there is still some debate as to whether there might remain some excess emission attributable to a distinct very hot diffuse component within a degree or so of the Galactic Centre (Uchiyama et al. 2011, 2013; Heard & Warwick 2013; Nishiyama et al. 2013). It has also been suggested recently that some fraction the GRXE might arise from the scattering of the radiation from bright Galactic X-ray binaries (XRBs) by the interstellar medium (Molaro et al. 2014).

One requirement on any Galactic source population (or populations) deemed responsible for GRXE is that the inferred volume emissivity should be sufficient to give rise to the observed surface brightness of the GRXE. A second constraint is that the

\* E-mail: rsw@le.ac.uk

integrated spectrum of the sources should match the observed GRXE spectrum. In this context it has been proposed that a mix of magnetic cataclysmic variables (CVs) plus coronally-active binaries may have sufficient spatial density and hard X-ray luminosity to account for the GRXE (Muno et al. 2004; Sazonov et al. 2006; Revnivtsev et al. 2006; Revnivtsev et al. 2008). Also, CVs and active binaries have marked spectral similarities to the GRXE (Revnivtsev et al. 2006; Tanaka & Yamauchi 2010; Yuasa et al. 2012). However current uncertainties relating to the population properties and statistics leave many of the details of this model to be confirmed.

One of the key elements in any source model of the GRXE is the underlying X-ray luminosity function (XLF) of the contributing sources, especially in the intermediate-to-low luminosity range (nominally  $10^{28-34}$  erg s<sup>-1</sup>). To date the best determination of the 2–10 keV XLF in this regime is that reported by Sazonov et al. (2006), based on the combination of *RXTE* and *Rosat* survey measurements. However, an obvious limitation of this work, which is particularly important for the coronally-active systems, was the need to extrapolate from the soft (0.1–2.4 keV) bandpass of *Rosat* into the hard 2–10 keV band. In this paper we remedy this situation by presenting a new determination of the 2–10 keV XLF based on a hard-band selected source sample derived from the *XMM-Newton* Slew survey (XSS; Saxton et al. 2008).

The remaining sections of this paper are organised as follows. In the next section we discuss the properties of a sample of low-luminosity Galactic X-ray sources detected in the XSS in the hard X-ray band. This sample comprises coronally-active stellar sources plus a smaller number of CVs (magnetic and non-magnetic). In §3 we use this XSS-derived source sample to determine a new estimate of the XLF of Galactic sources with 2–10 keV X-ray luminosities in the range  $10^{28-34}$  erg s<sup>-1</sup>. We go on (§4) to predict the form the Galactic X-ray source counts at Galactic longitude  $l = 28.5^\circ$  and compare the result with the available observational constraints. We also estimate the integrated X-ray emission due to faint Galactic X-ray sources and compare the result with the measured GRXE intensity (again at  $l = 28.5^\circ$ ). Finally, we discuss various aspects of our results in the context of the origin of the GRXE (§6) and then, summarize our conclusions (§7).

## 2 THE SOURCE SAMPLE DERIVED FROM THE XSS

*XMM-Newton* slews between successive pointings at a rate of 90° per hour. This results in an exposure time for X-ray sources lying on the slew path of typically between 1–10s. As reported by Saxton et al. (2008), based on such slew observations, the on-going XSS provides coverage of a significant fraction of the sky in a broad X-ray passband.

In the XSS data reduction, the source count rate measured in the EPIC pn camera through the medium filter is recorded in two nominal energy ranges, namely a soft (0.2–2 keV) band and a hard (2–12 keV) band. The limiting sensitivity for source detection in the hard band is approximately  $3 \times 10^{-12}$  erg cm<sup>-2</sup> s<sup>-1</sup> (2–10 keV). This is roughly an order of magnitude deeper than the ‘classical’ all-sky surveys which are currently available in this energy range, such as those from *Uhuru*, *Ariel V*, and *HEAO-1* (Forman et al. 1978; Warwick et al. 1981; McHardy et al. 1981; Piccinotti et al. 1982; Wood et al. 1984). Further details of the XSS can be found in Saxton et al. (2008).

In a recent paper, Warwick et al. (2012) analysed a sample of 487 sources detected in the XSS hard band within a survey

region encompassing 35% of the sky at high Galactic latitude ( $|b| > 10^\circ$ ). Through cross-correlation with multi-waveband catalogues, 47% of the XSS sources were found to have likely identifications with extragalactic sources (normal galaxies, active galaxies and clusters of galaxies) with a further 16% similarly identified with stellar sources (coronally-active stars and accreting binaries). Warwick et al. (2012) further concluded that many (perhaps the majority) of the remaining XSS sources with no obvious identification were likely to be spurious (a natural consequence of the low-significance threshold used to define the input sample).

Making use of the facilities afforded by VizieR<sup>1</sup>, and Simbad<sup>2</sup>, we have re-examined the 80 sources classed as “Stars” or “Other” in the XSS sample considered by Warwick et al. (2012). After excluding 11 sources associated with LMXB/HMXB in Local Group galaxies, 4 supernova remnants, an O star in Orion and 2 sources with no clearcut optical/NIR counterpart, we are left with a sample of 62 hard-band selected X-ray sources of likely Galactic origin. This set of objects (hereafter referred to as the *current* sample) includes 46 sources associated with coronally-active stars and binaries (ASBs) plus 16 probable CVs. All of these sources have a likely 2MASS<sup>3</sup> counterpart within or in close proximity to the X-ray error circle. Fig. 1 shows the distribution of the 2MASS  $K_s$  magnitude for the current sample and also the distribution of the NIR to X-ray position offsets.

### 2.1 The coronally-active stars and binaries

Table 1 summarises some of the properties of the 46 ASBs in the current sample. The columns of the table give the following information: the XSS catalogue name; the assumed distance; a reference to the distance estimate; the type of coronally-active system (if known); the name of the star or binary system; the spectral type of the star(s) comprising the system; the inferred (composite) absolute  $K_s$ -band magnitude ( $M_K$ ); an indication of whether the system includes either a giant or sub-giant star; the measured X-ray count rate in the XSS hard band and, finally, the inferred 2–10 keV X-ray luminosity ( $\log L_X$ ).

The  $M_K$  value is derived from the assumed distance and the 2MASS  $K_s$  measurement *without* application of any reddening correction (as the impact of reddening will be small for the great majority of the sources in this high-latitude sample). Similarly, the X-ray luminosity is determined from the quoted distance and the XSS hard-band count-rate based on the calibration,  $1 \text{ ct s}^{-1} = 6.2 \times 10^{-12} \text{ erg s}^{-1} \text{ cm}^{-2}$  (2–10 keV). Here we have assumed the source spectrum can be represented as a  $T = 35 \text{ MK}$  ( $kT = 3 \text{ keV}$ ) *apec* plasma with a metal abundance  $Z = 0.4 Z_\odot$ , subject to negligible line-of-sight absorption. This spectral form is reasonably compatible with the typical hard-to-soft count-rate ratio measured in the XSS for the ASB sample - as illustrated in Fig. 2 - although the scatter in this ratio is large. The underlying spectral characteristics of ASBs are discussed further in §6.

For the present study, the estimation of the source distance is key. Of the sources in Table 1, 29 have parallax measurements from Hipparcos (Perryman et al. 1997; van Leeuwen 2007a;

<sup>1</sup> <http://vizier.u-strasbg.fr/viz-bin/VizieR/>

<sup>2</sup> <http://simbad.u-strasbg.fr/simbad/>

<sup>3</sup> The Two Micron All Sky Survey (2MASS) (Cutri et al. 2003; Skrutskie et al. 2006) provides uniform coverage of the entire sky in three NIR bands, namely  $J$  (1.25  $\mu$ ),  $H$  (1.65  $\mu$ ) and  $K_s$  (2.17  $\mu$ ).

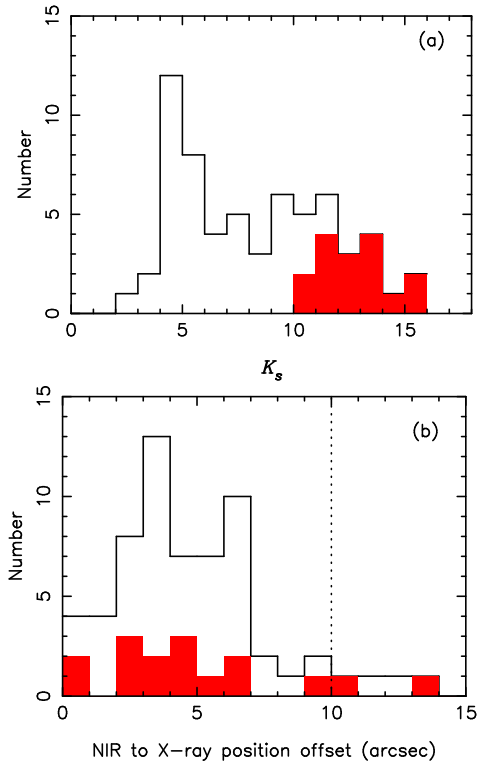


**Figure 1.** (a) The  $K_s$  magnitude distribution of the NIR counterparts to the sources in the current sample; the region shaded red corresponds to the CVs, with the remainder representing the ASBs. (b) The spatial offset between the 2MASS counterpart and the X-ray position; the red shading again corresponds to the CVs. The dotted vertical line is drawn at 10 arcsec and represents a nominal 90% X-ray error circle radius for the XSS (Warwick et al. 2012).

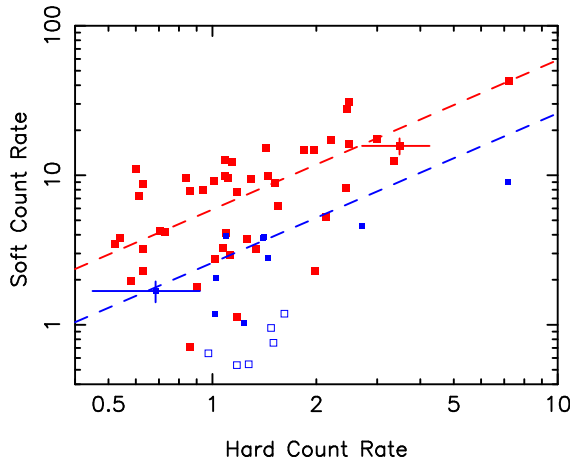


**Figure 2.** The XSS soft-band count rate plotted versus the XSS hard-band count rate for the ASBs (red points) and CVs (blue points) comprising the current sample. Upper-limit soft-band rates are identified by open symbols. Representative error bars are shown for two of the sources. The dashed lines illustrate the ratio of the hard-to-soft count rates predicted on the basis of the assumed ASB and CV spectral forms (see text).

van Leeuwen 2007b) and hence have a reasonably precise and unambiguous distance determination. Using the Hipparcos distance together with the  $J$  and  $K_s$  magnitudes from 2MASS (again without applying any correction for reddening), we can locate these 29 systems in the  $J - K_s$  colour versus absolute  $M_K$  magnitude plane, as illustrated in Fig. 3. Note that although the 2MASS photometry errors typically result in an error on the  $J - K_s$  colour of less than  $\sim 0.05$ , for 6 very bright stars (with  $K_s < 4.5$ ) saturation effects have presumably given rise to substantially higher uncertainties. Fig. 3 also shows the loci of dwarf and giant stars as derived from the stellar spectral-flux library compiled by Pickles (1998) (see their Tables 2 and 5), after applying the colour transformations (Bessell & Brett system to 2MASS) reported by Carpenter (2001). Evidently virtually all of the ASBs with Hipparcos distances lie within the band defined by these two loci (the one exception being the M3.5V star associated with XMMSL1 J184949.8-235011, which also happens to be the nearest star in the sample).

Based on information in the literature together with the source location in Fig. 3, we find that 16 out of the 29 coronally-active systems with Hipparcos distances most likely contain a giant or sub-giant star. Within the subset of 29 sources, there are 22 confirmed or probable binaries, comprising either RS CVn, BY Dra, W UMa or Algol type systems (Güdel 2004).

The 17 ASBs lacking Hipparcos parallaxes, as might be expected, tend to be the sources at fainter end of the  $K_s$  magnitude distribution. Using information in the literature we were able to classify 6 of these systems as likely containing late-K or M-dwarf stars<sup>4</sup>. A further source is a likely RS CVn binary containing a G7III star (Kiraga 2012). For these 7 systems we have either taken the distance estimate directly from the literature or estimated  $M_K$  from either the dwarf or giant locus in Fig. 3 (taking due note of the measured  $J - K_s$  colour). In the latter case the distance was then determined via the 2MASS  $K_s$  magnitude and a distance error range assigned assuming an uncertainty in  $M_K$  of 0.5 magnitude.

For the remaining 10 sources lacking parallax measurements the information in the literature relating to the spectral type, luminosity class and/or distance was very limited. Without any clear indication as to whether or not a given system contains a giant or sub-giant star, we set its  $M_K$  at the mid-value between the dwarf and giant loci in Fig. 3 (for the given  $J - K_s$  colour), with a preliminary error range in  $M_K$  equal to the separation of the two loci. The corresponding distance and the distance error range were then calculated from the observed  $K_s$  magnitude.

We have also compared the measured proper motion (largely taken from the PPMXL catalogue; Roeser et al. 2010) with the parallax inferred from the assigned distance - see Fig. 4. Using the 29 sources with Hipparcos measurements as a control sample to define the upper and lower bounds to the scatter in the proportionality between the two axes in Fig. 4, we were, at least in a few cases, able to set an additional constraint on the source distance. As a final step we also applied a limit to the distance upper-bound by restricting the inferred 2–10 keV X-ray luminosity for these coronal emitters to less than  $10^{32.5} \text{ erg s}^{-1}$ .

Table 1 reports the estimated distance and distance error range for each of the 17 ASBs lacking parallax measurements. The position of these 17 sources in the NIR colour-magnitude diagram is

<sup>4</sup> One of this group, the counterpart to XMMSL1 J160900.7-190846, may in fact be a pre-main sequence late-K dwarf star at the near-edge of the Upper Scorpius OB Association (Carpenter et al. 2009); on the basis of its extreme  $J - K_s$  colour this star appears to be significantly reddened.

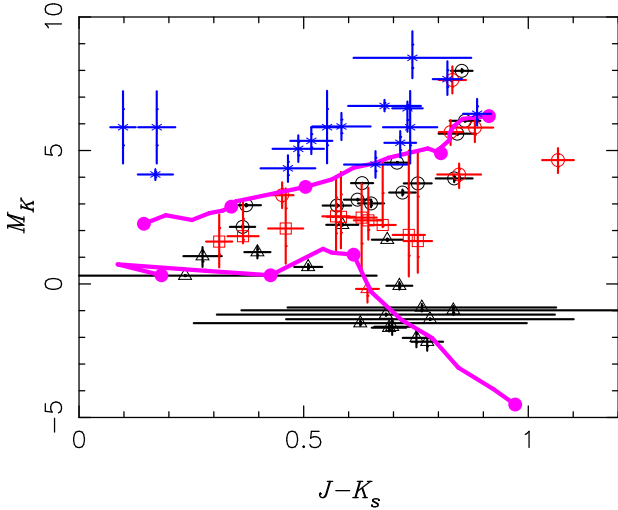


**Figure 3.** The absolute  $M_K$  magnitude versus the  $J - K_s$  colour for the NIR counterparts of the sources in the current sample. The ASBs with Hipparcos parallax measurements are shown as black symbols, with systems known to contain a giant (or sub-giant) star represented as triangles and the rest as circles. The ASBs without parallax measurements are shown as red symbols – known giants as triangles, known dwarf systems as circles and sources of uncertain type as squares. For the latter, the vertical red error bars encompass the uncertainty in the dwarf versus giant classification. The upper solid line corresponds to the locus of dwarf stars of spectral type F0 through to M5 (with the solid circles marking, from left to right, spectral types F0, G0, K0, M0 and M5). The lower solid line similarly corresponds to the locus of giant stars of spectral type F0 to M0 (with the solid circles marking, from left to right, spectral types F0, G0, K0 and M0). The blue asterisks symbols, plus associated error bars, represent the CVs in the current sample.

shown in Fig. 3, together with the commensurate final error bars on  $M_K$ .

As noted above, of the 29 systems with parallax measurements, 16, i.e. 55%, contain a giant or sub-giant star. In contrast the statistics for the systems without parallax measurements are 6 dwarfs, 1 (likely) giant and 10 of uncertain type. On the basis of this comparison, one might conclude that the majority of the latter are likely to be systems containing giant (or sub-giant) stars. Hence the procedure described above may lead to an underestimation of the distances (in a minority of cases) and hence a bias in the inferred distribution of X-ray luminosity. In this context, Fig. 5 shows the distribution of  $L_X$  for the ASBs divided into two subsets, namely those sources with or without Hipparcos parallax measurements. For the sources with Hipparcos-derived distances the measured  $L_X$  span the range  $10^{28-32} \text{ erg s}^{-1}$ , whereas for the remaining sources the  $L_X$  range extends to  $10^{32.5} \text{ erg s}^{-1}$  (consistent with the fact that the counterparts are typically somewhat fainter in the optical/NIR and are potentially more distant). The impact of an upward revision of  $L_X$  for the 10 sources where the dwarf versus giant classification is uncertain (to the  $L_X$  value corresponding to the quoted upper-bound on the distance) is also illustrated. The main result is an increase in the inferred number of systems with  $L_X > 10^{32} \text{ erg s}^{-1}$  from 5 to 7. In practice, this upward shift in  $L_X$  for a small number of sources will have only a minor impact on the inferred XLF of the sample of ASBs, taken as a whole (see §3).

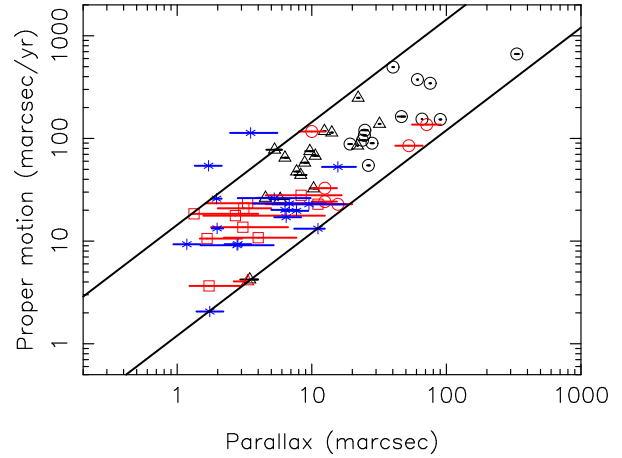


**Figure 4.** The proper motion in  $\text{marsec yr}^{-1}$  plotted against the parallax in  $\text{marsec}$  (measured or inferred) for the NIR counterparts of the sources in the current sample. The symbols are the same as in Fig. 3. The two diagonal lines represent nominal upper and lower bounds to the scatter and correspond to transverse velocities of 68 and  $5.7 \text{ km s}^{-1}$ , respectively.

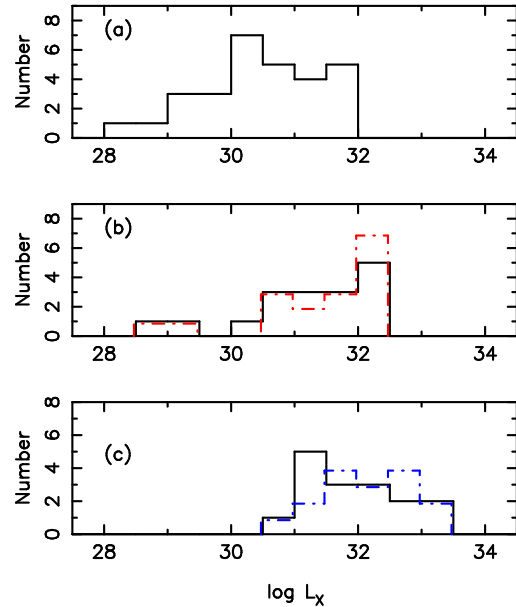


**Figure 5.** Panel (a): The distribution of X-ray luminosity for the ASBs with Hipparcos parallax measurements; (b): The same plot for the ASBs without Hipparcos parallax measurements. The dashed (red) histogram shows the impact of revising the source distance to the upper bound of its range in the case of the 10 sources for which the dwarf-to-giant classification is uncertain. Panel (c): The distribution of X-ray luminosity for the CVs. The dashed (blue) histogram shows the impact of revising all the CV distances to their upper bound.

## 2.2 The cataclysmic variables

Table 2 provides summary information relating to the 16 probable CVs in the current sample; the format is the same as in Table 1 except that the columns headed Spectral Type and Giant/sub-Giant are not included. Roughly half of this sample (7 out of 16) are known magnetic CVs, i.e. Polars (P) or Intermediate Polars (IP), as opposed to the non-magnetic Nova-like Variables (NL) or Dwarf Novae (DN).

The source distance is again the key information required in



**Table 1.** Details of the 46 sources in the current sample associated with ASBs.

XSS Name	Distance pc	Distance Reference	Type	Name	Spectral Type	$M_K$	Giant/sub-Giant	Hard Band ct s <sup>-1</sup>	log $L_X$ erg s <sup>-1</sup>
J011635.6-023003	81	(1)	RS CVn	AY Ceti	WD+G5IIIe	-1.1	Y	1.4	30.84
J012256.9+072509	45	(1)	RS CVn	AR Psc	K1IV+G7V	1.7	Y	1.8	30.44
J013500.9-295433	22	(1)	BY Dra	BB Sci	K3-4V+K4-5V	3.0	N	0.6	29.32
J023948.1-425302	36	(1)	late-MS	-	M2V	5.6	N	0.8	29.90
J024125.6+055916	42	(1)	late-MS	BD+05378	K6Ve	4.0	N	0.9	30.09
J024325.4-375544	41	(1)	BY Dra	UX For	G7V+K1V	2.9	N	1.3	30.20
J044118.7+205403	13	(1)	BY Dra	V834 Tau	K3Ve	4.5	N	0.6	28.91
J045100.6-121416	300 <sup>+80</sup> <sub>-0</sub>	(5)	RS CVn?	HD30900	G7III	-0.2	Y	1.2	31.90
J045330.4-555133	11	(1)	late-MS	GJ2036A	M3Ve	6.1	N	2.0	29.26
J045818.2-751638	289	(1)	FK Com	YY Men	K3IIIp	-2.0	Y	1.0	31.80
J050136.1-444949	94	(1)	FK Com	HD 32517	G8/K0III	0.6	Y	0.7	30.68
J050607.6-864153	64 <sup>+17</sup> <sub>-11</sub>	(2)	-	CPD-86 67	KV	4.1	N	1.3	30.58
J052845.4-652651	15	(1)	late-MS	AB Dor A	K0V	3.8	N	2.4	29.62
J054039.8-201759	221	(1)	RS CVn	TW Lep	F6IV+K2III	-2.2	Y	1.1	31.61
J062201.2-345448	250 <sup>+200</sup> <sub>-120</sub>	(5)	-	-	K	2.5	?	0.6	31.43
J063612.2+512258	80 <sup>+20</sup> <sub>-15</sub>	(5)	late-MS?	-	MV?	5.7	N	1.5	30.86
J070846.2+554905	580 <sup>+200</sup> <sub>-250</sub>	(5)	-	-	K	2.4	?	0.6	32.20
J081736.6-824336	14 <sup>+4</sup> <sub>-3</sub>	(2)	late-MS	-	M3.5V	5.9	N	0.6	28.95
J082730.0-672401	750 <sup>+30</sup> <sub>-500</sub>	(5)	-	-	K	2.2	?	0.6	32.42
J092225.6+401200	25	(1)	BY Dra	BF Lyn	K3V+K3V	3.2	N	1.1	29.71
J102146.8+605451	189	(1)	RS CVn	FG UMa	G9III	-1.6	Y	2.1	31.75
J130153.4-194631	121	(1)	Algol	UY Vir	A7V+G6IV	1.2	Y	3.4	31.56
J132132.4+385250	113	(1)	RS CVn	BM CVn	K2III	-0.9	Y	0.5	30.71
J133448.3+371058	46	(1)	RS CVn	BH CVn	F2IV+K2IV	0.3	Y	7.2	31.05
J143851.3+194500	19 <sup>+5</sup> <sub>-4</sub>	(3)	late-MS	-	M4V	7.6	N	0.9	29.36
J154547.5-302102	40	(1)	BY Dra	KW Lup	K2V	3.4	N	1.6	30.27
J155321.8-215817	172	(1)	Algol?	HD14209	A5V+?	1.0	Y	2.4	31.73
J160900.7-190846	80 <sup>+20</sup> <sub>-15</sub>	(4)	pre-MS?	-	K9	4.6	N	2.0	30.97
J171725.8-665712	31	(1)	RS CVn	V824 Ara	G7IV/V+K0IV/V	2.2	Y	2.5	30.26
J173240.2+741335	104	(1)	RS CVn	DR Dra	WD+K0III	-1.0	Y	1.1	30.94
J175757.9+042732	600 <sup>+80</sup> <sub>-270</sub>	(5)	-	-	G	1.8	?	0.9	32.38
J182509.4+645018	159	(1)	RS CVn?	HD170527	K0 (III?)	-1.6	Y	1.1	31.30
J183355.8+514306	16	(1)	By Dra	By Dra	K6Ve+K7V	3.8	N	1.4	29.46
J183419.9+184126	38	(1)	By Dra	V889 Her	G2V	2.9	N	1.1	30.07
J184949.8-235011	3.0	(1)	late-MS	V1216 Sgr	M3.5Ve	8.0	N	2.2	28.17
J190825.4+522529	71	(1)	RS CVn	V1762 Cyg	K2IV-III+G8V	-1.3	Y	2.5	30.97
J195518.4+734933	325 <sup>+235</sup> <sub>-175</sub>	(5)	-	-	G/K	2.5	?	1.3	32.02
J200030.9+592135	100 <sup>+25</sup> <sub>-20</sub>	(5)	-	-	GV	3.3	N	3.5	31.41
J203654.3-465758	300 <sup>+315</sup> <sub>-230</sub>	(5)	-	-	K	1.8	?	0.7	31.67
J203722.8+705720	320 <sup>+180</sup> <sub>-120</sub>	(5)	-	-	F	1.6	?	0.9	31.82
J204542.4+042141	120 <sup>+100</sup> <sub>-60</sub>	(5)	-	-	G	2.1	?	1.1	31.07
J210225.8+274823	52	(1)	W UMa	ER Vul	G0V+G5V	2.1	N	1.1	30.36
J214126.5-104750	370 <sup>+270</sup> <sub>-290</sub>	(5)	-	-	K	1.6	?	1.0	32.02
J215627.2+051600	90 <sup>+130</sup> <sub>-40</sub>	(5)	-	-	K	2.5	?	0.5	30.50
J231323.5+024033	97	(1)	RS CVn	SZ Psc	F8IV+K1IV	-0.1	Y	3.0	31.32
J234941.1+362531	130	(1)	FK COM	OU And	G1IIIe	-1.5	Y	1.2	31.17

**References:** (1) Hipparcos parallax measurement - van Leeuwen (2007a); (2) Riaz et al. (2006); (3) Lepine & Gaidos (2011); (4) Distance set at the lower limit of the range quoted by de Zeeuw et al. (1999) for Upper Sco. Association ; (5) this paper.

the calculation of the XLF. Distance estimates and error bounds are available from the literature (see the table for the references) for 12 of the sources, including 5 based on the period-luminosity-colour prescription employed by Ak et al. (2008). For the 4 sources lacking relevant information we have calculated the distance from the observed 2MASS  $K_s$  magnitude assuming  $M_K = 5.9 \pm 1.3$ , representing the mean  $M_K$  and standard deviation of the  $M_K$  distribution of the 12 other sources.

In the colour-magnitude plane of Fig. 3, the CVs in general occupy the region above the locus of dwarf stars. In Fig. 4 the

CVs are mostly located in same band as the ASBs, the two exceptions being RBS 490 and TX Col. The anomalously-high transverse velocity implied for RBS 490 has previously been noted by Thorsensen et al. (2006).

The last two columns of Table 2 give the measured X-ray count rate in the XSS hard band and the X-ray luminosity (log  $L_X$ ) determined from this count rate and the assumed distance. Here we employ the calibration  $1 \text{ ct s}^{-1} = 7.9 \times 10^{-12} \text{ erg s}^{-1} \text{ cm}^{-2}$  (2–10 keV). This is based on the assumption that the CV source spectrum can be approximated as a  $kT = 10 \text{ keV}$  thermal bremsstrahlung

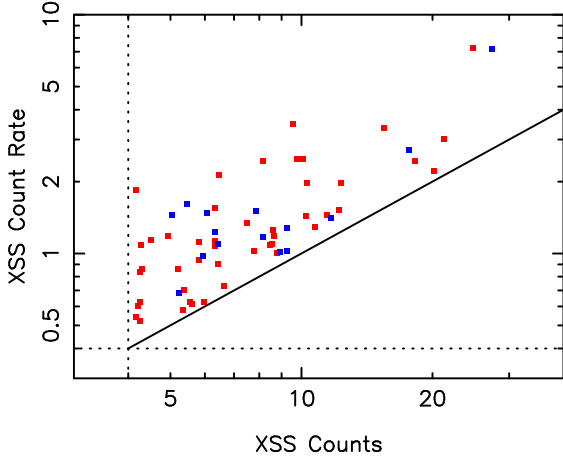


**Figure 6.** The XSS hard-band count rate (in  $\text{ct s}^{-1}$ ) plotted versus the net counts (after background subtraction) recorded in the XSS hard band. The ASBs and CVs are represented by the red and blue points, respectively. The vertical and horizontal dashed lines correspond to the criteria applied in constructing the current sample, namely  $\geq 4$  net counts and  $\geq 0.4 \text{ ct s}^{-1}$ . The solid diagonal line illustrates the relationship between counts and count rate for a nominal 10 s exposure time, which is close to the maximum in the XSS. For all the sources in the current sample, the net-count limit will always be encountered (as the source distance is increased) before the minimum count-rate threshold is reached. Hence the current sample can be described as count-limited.

spectrum subject to absorption in a line-of-sight column density of  $5 \times 10^{20} \text{ atom cm}^{-2}$ ; in fact, Fig. 2 suggests that this spectrum is representative of the minimum spectral hardness exhibited by the CV sample. The values of  $L_X$  so determined span the range  $10^{30.5-33.5} \text{ erg s}^{-1}$  - as illustrated in Fig. 5. Finally, the potential impact of the uncertainties in the CV distances has been tested by revising all the distance estimates to the upper bound quoted in Table 2 and recalculating  $L_X$ . As is evident from Fig. 5, this results in a marginal upward shift in the centroid of  $L_X$  distribution. However, in the context of the CV XLF (discussed in §3), this is not a significant effect.

### 3 2-10 KEV X-RAY LUMINOSITY FUNCTIONS

We have made use of the current sample to construct the differential XLF in the 2–10 keV band of the ASBs and CVs. As noted earlier, the range of  $L_X$  sampled spans roughly six decades from  $10^{28-34} \text{ erg s}^{-1}$ . For a flux-limited survey it is possible to estimate the space density of sources in a given  $L_X$  range using the  $1/V_{\text{max}}$  method (Schmidt 1968). In this approach, the distance  $d_{\text{max}}$  at which a source would reach a given flux-limit is calculated on the basis of the *measured* source flux and the known source distance. The survey volume  $V_{\text{max}}$  is then determined by integrating over the solid angle of the survey, taking into account any variations in the flux-limit across the region. However, in the present work it was necessary to modify this approach since the dominant selection criterion is a *net counts* threshold rather than a specific count-rate threshold (the latter being akin to a flux limit) - as explained in Fig. 6. Our calculation of  $d_{\text{max}}$ , therefore, makes use of the minimum count criterion of the survey, namely net 4 counts in the XSS hard band, along with the measured net counts in this band registered for each source.

A further consideration is that we are dealing with Galactic source populations which will show a spatial concentration towards

the Galactic plane. Assuming the space density of the sources declines as  $\exp(-|z|/h)$ , where  $z$  is the distance above or below the Galactic plane and  $h$  is the population scale height, then the contribution to the volume integral of a survey region of solid angle  $\delta\Omega$  varies with Galactic latitude  $b$  as:

$$\delta V_{\text{max}} = \delta\Omega \frac{h^3}{\sin |b|^3} [2 - (\xi^2 + 2\xi + 2)e^{-\xi}]$$

where  $\xi = d_{\text{max}} \sin |b|/h$  (Tinney et al. 1993; Sazonov et al. 2006; Pretorius & Knigge 2012; Pretorius et al. 2013).

In the present analysis we assume  $h = 150 \text{ pc}$  for both the ASBs and CVs. Sazonov et al. (2006) make the same assumption and note that, for their sample of ASBs, the inferred space density is not very sensitive to the scale-height estimate, since the majority of the sources are observed at  $z < 150 \text{ pc}$  (i.e. less than 1 scale height). For our current sample, 87 per cent of the ASBs have inferred  $z$ -distances less than 150 pc, whereas for the CVs, the fraction is 75 per cent. By way of comparison, Pretorius & Knigge (2012) and Pretorius et al. (2013) use scale height estimates of 120 pc for long-period CVs and 260 pc for short period systems. We have investigated the impact of different scale height assumptions in the present work; taking  $h = 120 \text{ pc}$  (200 pc), instead of 150 pc, changes the inferred space density of the ASBs by a factor of 1.1 (0.9), whereas for the CVs the factor is 1.25 (0.75).

We have calculated  $V_{\text{max}}$  for each source by summing the  $\delta V_{\text{max}}$  increments over the high latitude sky ( $|b| > 10^\circ$ ), assuming the coverage fraction of the XSS is 35% (Warwick et al. 2012). As a check of the validity of this process we have also calculated  $V/V_{\text{max}}$  for each source (where  $V$  is the volume obtained when the source distance  $d$  is substituted for  $d_{\text{max}}$  in the volume calculation). For the sample as a whole, the distribution of  $V/V_{\text{max}}$  is reasonably uniform over the range 0–1 with an average  $\langle V/V_{\text{max}} \rangle = 0.514 \pm 0.031$ , consistent with the expectation for a homogeneous and uniform population.

We have determined the source space density as  $\sum(1/V_{\text{max}})$ , where the summation is over all the sources contributing to a particular  $L_X$  bin. In this context, although the total number of sources in the current sample is relatively small, it has proved useful to derive separate XLFs for the ASBs and CVs. The resulting differential XLFs in the 2–10 keV band (employing logarithmic  $L_X$  bins) are shown as the two sets of points plotted in Fig. 7. In this figure the y-axis has been scaling by the factor  $L_X/\rho_0$  where  $\rho_0$  is the stellar mass density in the solar neighbourhood. Mirroring the approach used by Sazonov et al. (2006), we set  $\rho_0 = 0.04 \text{ M}_\odot \text{ pc}^{-3}$ . For the ASBs, we have utilized seven log  $L_X$  bins encompassing the range  $10^{28-32.5} \text{ erg s}^{-1}$ , whereas for the CVs we use four such bins covering the range  $10^{30-34} \text{ erg s}^{-1}$ .

We have fitted the central segment of each XLF with a power-law function of the form:

$$\frac{dN}{d \log L_X} = K_{31} (L_X/L_{31})^{-\alpha}$$

where  $\alpha$  is slope of the power-law and  $K_{31}$  represents the normalization (scaled by  $\rho_0^{-1}$ ) measured at an X-ray luminosity  $L_{31} = 10^{31} \text{ erg s}^{-1}$ . However, in order to match the observed data, this power-law was modified, in the case of the ASBs, by downward breaks (with  $|\Delta\alpha| = 1$ ) at both the low end and high end (more specifically at luminosities of  $10^{29}$  and  $10^{32} \text{ erg s}^{-1}$ , respectively). The XLF of the CVs was fitted similarly, but in this case with only a low-end break at  $L_X = 10^{31} \text{ erg s}^{-1}$ .

For the ASBs, trial fits of the doubly-broken power-law function (varying  $\alpha$  with  $K_{31}$  as a free parameter) indicated a best-

**Table 2.** Details of the 16 sources in the current sample associated with CVs

XSS Name	Distance pc	Distance Reference	Type	Name	$M_K$	Hard Band $\text{ct s}^{-1}$	$\log L_X \text{ erg s}^{-1}$
J014448.4+323258	$147^{+128}_{-68}$	(1)	NL	BG Tri	5.9	1.2	31.40
J035410.3-165252	$285^{+120}_{-105}$	(2,3)	P	RBS 490	8.5	0.7	31.72
J040910.7-711739	$64^{+20}_{-17}$	(3)	DN	VW Hyi	7.7	1.1	30.63
J053450.9-580136	$848^{+219}_{-175}$	(4,5)	IP?	TW Pic	4.5	2.7	33.26
J054320.1-410201	$585^{+155}_{-118}$	(4,6)	IP	TX Col	4.3	1.5	32.69
J061145.1-814925	$158^{+42}_{-33}$	(4,7)	NL	AH Men	5.9	1.0	31.36
J062339.6-265750	$190^{+165}_{-88}$	(1)	DN?	-	5.9	1.4	31.68
J062516.3+733439	$573^{+146}_{-119}$	(4)	IP	MU Cam	5.1	1.0	32.50
J082513.7+730639	$130^{+37}_{-24}$	(8)	DN	Z Cam	5.3	1.2	31.27
J082623.4-703143	$90^{+45}_{-10}$	(9)	DN?	-	6.6	1.4	31.03
J114336.8+714125	$155^{+35}_{-35}$	(4,10)	IP	DO Dra	6.4	1.4	31.52
J130057.6-491211	$105^{+91}_{-49}$	(1)	DN	V1147 Cen	5.9	1.6	31.23
J173022.3-055935	$359^{+313}_{-167}$	(1)	IP	V2731 Oph	5.9	1.3	32.19
J185502.6-310937	$510^{+52}_{-43}$	(11)	IP	V1223 Sgr	4.1	7.2	33.25
J190715.9+440105	$505^{+50}_{-31}$	(12)	NL	MV Lyr	6.7	1.5	32.55
J194904.4+774424	$354^{+91}_{-73}$	(4)	DN	AB Dra	5.4	1.0	32.08

**References:** (1) Assumes  $M_K = 5.9 \pm 1.3$ , this paper; (2) Thorsensen et al. (2006); (3) Pretorius & Knigge (2012); (4) Ak et al. (2008); (5) Norton et al. (2000); (6) Buckley & Tuohy (1989); (7) Gänsicke & Koester (1999); (8) Thorsensen (2003); (9) Parisi et al. (2012); (10) Pretorius et al. (2013); (11) Beuermann et al. (2004); (12) Hoard et al. (2004).

fitting slope of  $\alpha = 1.21 \pm 0.05$  ( $1\sigma$  errors). Since the error range encompasses  $\alpha = 1.22$ , the value adopted by Sazonov et al. (2006), as an aid to comparison we have fixed  $\alpha$  at this value for the ASBs. In the case of the CVs the error range on  $\alpha$  was wider but again encompassed 1.22, so the XLF slope was also fixed at this value for the CVs.

The best-fitting normalizations of the XLF for the ASBs was determined to be  $K_{31} = 1.88 \times 10^{-4} \text{ M}_{\odot}^{-1}$  with a fitting uncertainty of roughly 15%, whereas for the CVs the value was  $K_{31} = 1.15 \times 10^{-4} \text{ M}_{\odot}^{-1}$  to a precision of roughly 25%. These are factors of  $2.1 \pm 0.3$  and  $1.3 \pm 0.3$  higher than the normalization quoted by Sazonov et al. (2006), for their combined XLF of ASBs and CVs. The best-fitting broken power-law models of the XLFs are shown in Fig. 7, in comparison with the XLF derived by Sazonov et al. (2006).

The inferred local space density for the ASBs obtained by integrating over the full XLF is  $3.4 \pm 0.5 \times 10^{-3} \text{ pc}^{-3}$ . This is higher than the space density reported by Sazonov et al. (2006) due to both the upward shift in the XLF normalization and the extension of the XLF power-law to a lower break luminosity. The inferred local space density of the CVs is  $3.4 \pm 0.7 \times 10^{-5} \text{ pc}^{-3}$  which is toward the top end of the (albeit wide) range of previous estimates (e.g. Pretorius & Knigge 2012 and references therein).

An upward trend is also evident in the integrated X-ray emissivities. From the XLFs in Fig. 7 we obtain a 2-10 keV X-ray emissivity, scaled to the local stellar mass density, of  $1.08 \pm 0.16 \times 10^{28} \text{ erg s}^{-1} \text{ M}_{\odot}^{-1}$  for the ASBs and  $2.5 \pm 0.6 \times 10^{27} \text{ erg s}^{-1} \text{ M}_{\odot}^{-1}$  for the CVs. For comparison, Sazonov et al. (2006) quote a value of  $4.6 \pm 0.9 \times 10^{27} \text{ erg s}^{-1} \text{ M}_{\odot}^{-1}$  for ASBs (including young coronally-active stars) and CVs combined, whereas Revnivtsev & Molokov (2012) determine a total 2-10 keV emissivity of  $3.0 \pm 0.3 \times 10^{27} \text{ erg s}^{-1} \text{ M}_{\odot}^{-1}$  from an *RXTE* scan across the Galactic plane at  $l = 18.5^\circ$ . The clear conclusion from the current analysis is that ASBs make a more significant contribution to the hard-band source statistics than previously recognised.

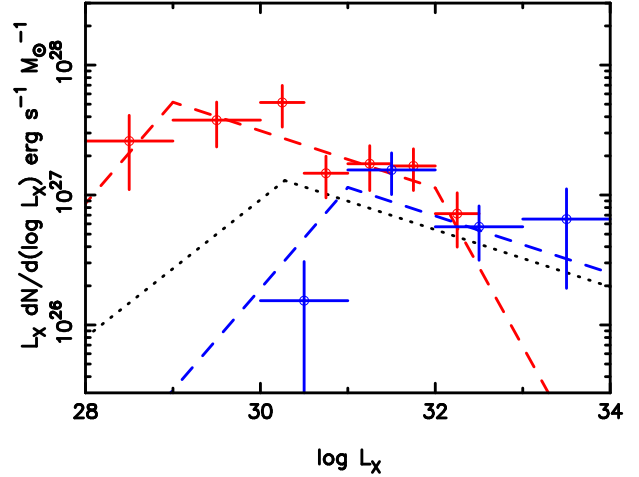


**Figure 7.** The differential XLF in the 2–10 keV band for the ASBs (red points) and the CVs (blue points), scaled by  $L_X$  and normalized to the local stellar mass density (see text). The blue and red dashed lines represent the best-fitting broken power-law fits to the data points. The black dotted line shows the combined XLF for ASBs and CVs derived by Sazonov et al. (2006).

## 4 X-RAY SOURCE COUNTS ON THE GALACTIC PLANE

### 4.1 Predicted Source Counts

In this section we use our newly determined XLFs to investigate the contribution of ASBs and CVs to the 2–10 keV X-ray source counts (i.e. the  $\log N - \log S$  curve) measured in the Galactic plane. Specifically, we focus on the direction  $(l, b) = (28.5^\circ, 0^\circ)$  for which the best observational constraints are available (outside of the Galactic Centre region).

We assume that the current XLFs (which reflect the space density of sources within 1 kpc of the Sun) apply across the whole of

the Galactic disc, albeit with a normalization which scales with the local stellar mass density  $\rho_{\text{gal}}$ . In the current work we estimate the latter using a mass model for the Galactic disc of the form (Revnivtsev & Sazonov 2007):

$$\rho_{\text{gal}}(R) \propto \exp[-(R/R_{\text{m}})^{-3} - (R/R_{\text{disk}})]$$

where  $R$  is Galactocentric radius,  $R_{\text{disk}}$  is the exponential scale-length within the Galactic disc and  $R_{\text{m}}$  represents an inner cutoff to the disc, interior to which the Galactic bulge and bar dominate. As noted by Revnivtsev & Sazonov (2007), for  $l = 28.5^\circ$  the contribution of the bulge/bar is likely to be small and hence only the disc component need be considered. We further note that the above expression does not include a dependence on  $z$  and the  $z$ -scale height of the population, since we restrict our source count calculation to a direction on the Galactic plane. Following Revnivtsev & Sazonov (2007) we take  $R_{\text{disk}} = 2.2$  kpc,  $R_{\text{m}} = 2.5$  kpc and further assume that the stellar mass density drops to zero for  $R > 10$  kpc. The scale factor applied to the XLF at locations along the line of sight is then  $\rho_{\text{gal}}(R)/\rho_{\text{gal}}(R_{\text{sol}})$ , taking the distance to the Galactic centre,  $R_{\text{sol}}$ , to be 8 kpc. As illustrated in Fig. 8(a), for the specified direction, this scale factor reaches a maximum value of  $\approx 5$  at the tangent point (near 7 kpc) and thereafter declines until the ‘disc edge’ (at  $R = 10$  kpc) is encountered at a line-of-sight distance of 15.8 kpc.

Using the scaled XLFs, it is straightforward to calculate the *unabsorbed* flux distribution of the sources contained within a given volume element at a given distance. The conversion to observed (i.e. absorbed) flux then requires a model for the absorption along the line of sight. Here, for simplicity, we assume the X-ray absorption arises from interstellar gas with a solar metal abundance and a density in the Galactic disc which scales as the stellar-mass density. The gas density is normalized to a solar-neighbourhood value of  $0.4 \text{ atom cm}^{-3}$ . The line of sight through the Galactic plane out to 15.8 kpc, then intercepts a total column density of  $5.8 \times 10^{22} \text{ atom cm}^{-2}$ , consistent with earlier estimates (Ebisawa et al. 2001; Ebisawa et al. 2005). The reduction in the 2–10 keV flux due to absorption is plotted as a function of the source distance in Fig. 8(b). Here, the transmission factors were calculated using WebPIMMS<sup>5</sup>, assuming the spectral forms for the ASBs and CVs detailed in §2. The somewhat softer spectra assumed for the ASBs compared to the CVs, results in the lower transmission factors evident in Fig. 8(b). Our absorption model predicts a flux transmission factor of 0.57 for an ASB observed at the far edge of the Galactic disc, compared to a value of 0.68 for a CV.

Using the methodology outlined above, we have carried out an integration along the line of sight to determine the source number versus flux relation for both the ASB and the CV populations. However, to complete the picture we need to include two further contributions, namely that of Galactic XRBs and extragalactic X-ray sources.

For the XRBs we use a differential XLF similar to that discussed by Sazonov et al. (2006) encompassing the range  $L_{\text{X}} = 10^{34-38} \text{ erg s}^{-1}$ . More specifically, we assume an XLF with  $\alpha = 0.25$  up to  $L_{\text{X}} = 1.7 \times 10^{37} \text{ erg s}^{-1}$  at which point the slope steepens to  $\alpha = 0.9$ . The normalization at the break point was set at  $2.6 \times 10^{-9} M_{\odot}^{-1}$ . The absorption versus distance relation was taken to be the same as for the CVs. The result was a good match

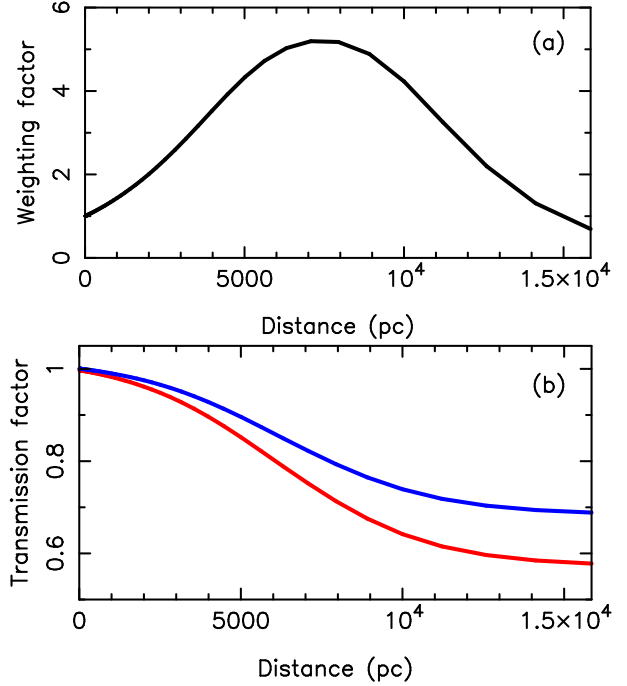


**Figure 8.** (a) The XLF scale factor as derived from the model of the stellar mass density in the Galactic disc plotted as a function of the line-of-sight distance in the direction  $(l, b) = (28.5^\circ, 0.0^\circ)$ . (b) The transmission versus distance for X-ray sources in the Galactic plane for the same line of sight. The values apply to fluxes measured in the 2–10 keV band. The red curve corresponds to the ASBs and the blue curve to the CVs.

to the high flux end of the observed Galactic source counts as discussed in §4.2.

For the extragalactic sources, we use the empirical formula representing the source counts in the 2–10 keV band reported by Moretti et al. (2003). In this case we adjusted the flux scale by a factor of 0.68 to account for the foreground absorption in the Galactic plane.

The predicted number of sources is plotted versus the limiting 2–10 keV flux ( $S_{\text{X}}$ ) in Fig. 9(a). As expected luminous XRBs dominate the integral counts at the high-flux end. CVs become the numerically dominant population at intermediate fluxes, or more precisely in the flux decade below  $S_{\text{X}} = 5 \times 10^{-13} \text{ erg cm}^{-2} \text{ s}^{-1}$ . Thereafter the integral counts are dominated by the extragalactic sources until the ASBs come to the fore below  $S_{\text{X}} \approx 3 \times 10^{-15} \text{ erg cm}^{-2} \text{ s}^{-1}$ . These crossover points are further illustrated in the Fig. 9(b), which shows the corresponding  $\log N(>S_{\text{X}})$  versus  $\log S_{\text{X}}$  relation normalized to the function  $(S_{\text{X}}/10^{-14})^{-1.5}$  (i.e. a source count relation with the *Euclidean* slope). At the lower flux boundary in Fig. 9(a), the predicted number of ASBs per square degree is in excess of  $2 \times 10^6$ . At the far edge of the Galaxy, stars with  $S_{\text{X}} = 10^{-18} \text{ erg cm}^{-2} \text{ s}^{-1}$  have an intrinsic 2–10 keV X-ray luminosity of  $\approx 5 \times 10^{28} \text{ erg s}^{-1}$ , implying that the number counts of such systems will rapidly tail off at even fainter fluxes (provided, of course, the inferred low-end break in the XLF of the ASBs is real).

## 4.2 Comparison with Observations

In recent times, X-ray observatories have surveyed many segments of the low-latitude sky resulting in the detection of large numbers of X-ray sources over a wide flux range (e.g. Munro et al. 2003; Munro et al. 2006; Revnivtsev & Sazonov 2007; Revnivtsev et al.

<sup>5</sup> <http://heasarc.gsfc.nasa.gov/Tools/w3pimms.html>



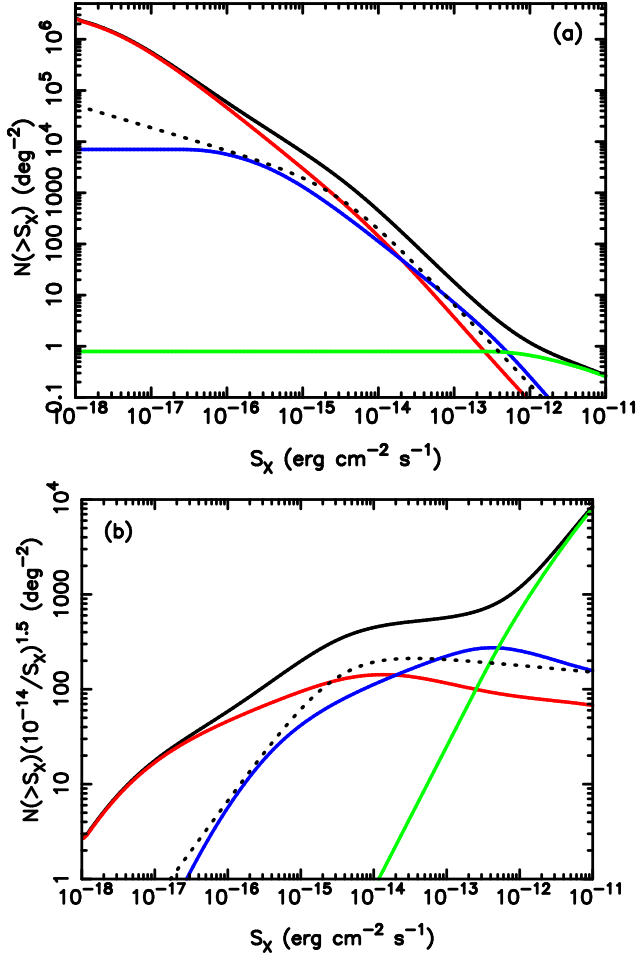


**Figure 9.** (a) The predicted integral source counts in the 2–10 keV band. The number of sources observed down to a given 2–10 keV flux threshold  $S_X$  is plotted versus  $S_X$ . The different curves represent: the ASBs (red); the CVs (blue); the XRBs (green); the extragalactic sources (dotted black) and the combined counts (solid black). (b) The predicted integral source counts in 2–10 keV band normalized to the Euclidean form, i.e. to the function  $(S_X/10^{-14})^{-1.5}$ . The curve representations are the same as in (a). These predictions pertain to the direction  $(l, b) = (28.5^\circ, 0.0^\circ)$ .

2011; Morihana et al. 2013; Nebot Gómez-Morán et al. 2013). Here we focus on three observational datasets, which may be reasonably compared with our source count predictions for the direction  $(l, b) = (28.5^\circ, 0.0^\circ)$ . The first stems from the extensive survey encompassing the inner quadrant of the Galactic plane carried out by ASCA (Sugizaki et al. 2001). The second relates to the *XMM-Newton* Galactic Plane Survey (XGPS), which covered a narrow strip of the plane between  $l = 19^\circ - 22^\circ$  (Hands et al. 2004). Although not specifically aligned with our target direction, these surveys nevertheless provide very useful source detection statistics in the flux range from  $10^{-11} \text{ erg cm}^{-2} \text{ s}^{-1}$  down to roughly  $3 \times 10^{-14} \text{ erg cm}^{-2} \text{ s}^{-1}$  (2–10 keV). The limits on the Galactic log  $N - \log S$  relation resulting from these two surveys are shown in Fig. 10.

A pair of deep ( $\sim 100$  ks), partly overlapping Chandra ACIS-I observations targeted at the plane near  $l = 28.5^\circ$  provide important additional constraints. In these observations X-ray sources were detected with fluxes down to  $\approx 3 \times 10^{-15} \text{ erg cm}^{-2} \text{ s}^{-1}$  (2–10 keV), thus extending the source counts a decade below that accessible via the XGPS programme. Ebisawa et al. (2005) have carried out a de-

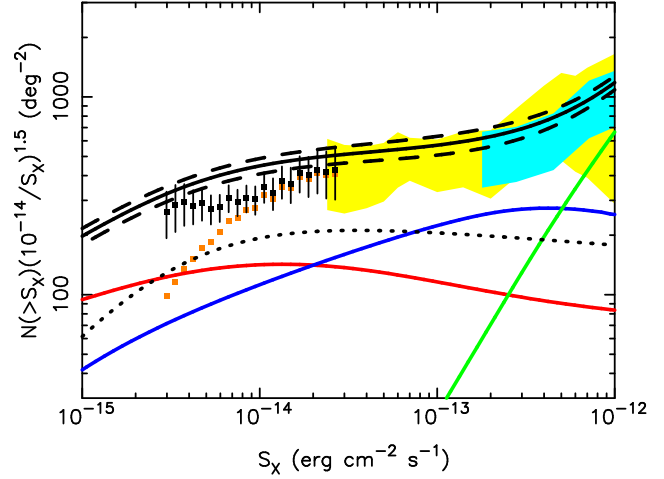


**Figure 10.** The 2–10 keV Galactic log  $N - \log S$  relation, normalized to the function,  $(S_X/10^{-14})^{-1.5}$ . The light blue and yellow shaded regions show the constraints derived from the ASCA and XGPS surveys, respectively. The data points show the number counts from two deep ( $\sim 100$  ks) Chandra observations, both before (brown squares) and after (black points with error bars) applying a coverage correction - see text. The curves have the same representation as in Fig. 9(a). The combined (i.e. total) counts (solid black curve) is shown with upper and lower error bounds (dashed black curves).

tailed study of these Chandra observations including the identification, where possible, of NIR counterparts to the X-ray sources. A interesting result from the Ebisawa et al. (2005) study (see also Ebisawa et al. 2001) was that the observed number density of X-ray sources, at the survey sensitivity limit, is  $\sim 600$  sources per square degree. These authors further note that this measured source density is comparable to that predicted for extragalactic sources, after making due allowance for the impact of the foreground absorption in the Galactic plane. Since this implied rather tight constraints on the residual contribution of Galactic sources at these faint fluxes, Ebisawa et al. (2005) concluded that the bulk of the GRXE must be of diffuse origin. Unfortunately, these conclusions are contrary to the predictions based on our newly-derived XLFs for low-luminosity Galactic X-ray sources.

To address this issue, we have re-assessed the spatial density of the faint sources detected in the *Chandra* observations considered by Ebisawa et al. (2005). We take as the starting point the set of hard (3–8 keV) band detections reported by Ebisawa et al. (2005) (see their Table 1). There are, in fact, 78 point sources detected in this band with a significance of  $\geq 4\sigma$ . We convert the vignetting-corrected hard-band count rates of these objects to a 2–10 keV flux assuming the calibration  $1 \text{ ct } (100 \text{ ks})^{-1} = 4 \times 10^{-16} \text{ erg cm}^{-2} \text{ s}^{-1}$ . The application of a flux threshold of  $3 \times 10^{-15} \text{ erg cm}^{-2} \text{ s}^{-1}$  (2–10 keV) then results in the exclusion of 1 source from the sample. The implied sky density is 606 sources per square degree (taking the sky area covered by the pair of overlapping fields to be  $0.127 \text{ deg}^2$ ); this (raw) estimate is fully consistent with the values reported by Ebisawa et al. (2001) and Ebisawa et al. (2005). However, this analysis neglects the corrections which must be applied for the varying sensitivity across the Chandra field of view.

We have estimated a coverage correction (e.g. Munro et al. 2003; Bauer et al. 2004; Morihana et al. 2013) appropriate to the pair of *Chandra* observations using the sensitivity map estimator

provided in conjunction with the Chandra Source Catalog<sup>6</sup>. Specifically, we used this tool to determine the point source detection sensitivity (in units of photon  $\text{cm}^{-2} \text{s}^{-1}$ ) in the *Chandra* H (2–7 keV) band for locations on a  $0.02^\circ \times 0.02^\circ$  square grid covering the combined fields of view of the *Chandra* observations. These results were then combined to produce a coverage curve (i.e. the fraction of the survey reaching a given sensitivity threshold), against which the effective survey area for each source could be determined (assuming the further calibration  $1 \text{ ct} (100 \text{ ks})^{-1} = 4 \pm 0.4 \times 10^{-8} \text{ photon cm}^{-2} \text{s}^{-1}$  in the 2–7 keV band).

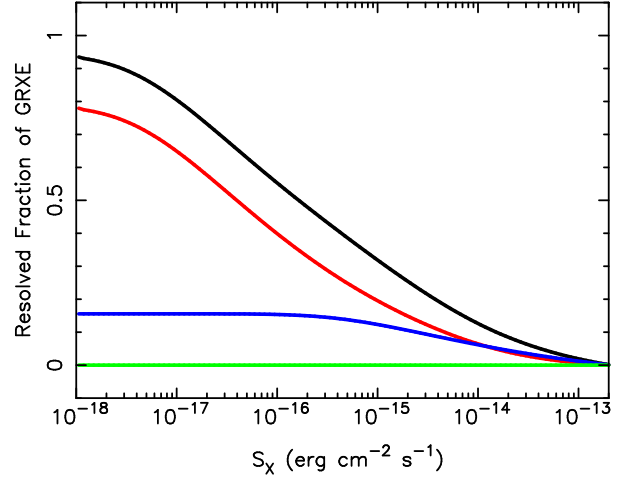
The resulting source counts both before and after apply this coverage correction are shown in Fig. 10. At the faint flux limit, the number density of the *Chandra* sources rises to  $1610 \pm 425 \text{ deg}^{-2}$  after correction (with the relatively large error bar reflecting uncertainties in the coverage correction process). This is well in excess of the number density of extragalactic sources predicted at  $S_X = 3 \times 10^{-15} \text{ erg cm}^{-2} \text{s}^{-1}$  ( $\sim 700 \text{ deg}^{-2}$ ). The conclusion that the  $\log N - \log S$  curve of Galactic X-ray sources continues to rise rapidly in the faint flux regime, is also consistent with the number counts reported by Revnivtsev & Sazonov (2007), albeit for sources selected in the softer 1–7 keV band.

Fig. 10 shows the full set of constraints derived from the observational datasets, in comparison with our estimates for each class of source and the predicted total source count. Upper and lower error bounds to the latter are also indicated; these were calculated assuming a 15 per cent uncertainty on the normalization of the ASB number counts, 25 per cent in case of the CVs, and 10 per cent for both the XRBs and extragalactic sources (all added in quadrature). In general, the observed source number count and predicted total counts are in good agreement. One caveat is, perhaps, that the *Chandra* data show a small deficit, relative to the total count prediction, at  $S_X \approx 10^{-14} \text{ erg cm}^{-2} \text{s}^{-1}$ . At this flux limit the number of sources actually *observed* in the pair of *Chandra* fields is 37 compared to a *predicted* number of  $48.0 \pm 4.3$ ; the difference amounts to a  $1.5\sigma$  effect.

## 5 CONTRIBUTION TO THE GRXE

Recent observations with *Suzaku* have added significantly to our knowledge of the surface brightness distribution and spectral properties of the GRXE (e.g. Yamauchi et al. 2009; Uchiyama et al. 2013). In the context of the present work, the study carried out by Ebisawa et al. (2008) is particularly valuable in providing a precise measurement of the absolute X-ray surface brightness in the direction  $(l, b) = (28.46^\circ, -0.20^\circ)$ . Ebisawa et al. (2008) report that, after excluding point sources brighter than  $\approx 2 \times 10^{-13} \text{ erg cm}^{-2} \text{s}^{-1}$  (2–10 keV), the total sky brightness in the 2–10 keV band is  $6.1 \times 10^{-11} \text{ erg cm}^{-2} \text{s}^{-1} \text{deg}^{-2}$ . After allowing for the contribution of the (extragalactic) cosmic X-ray background, the resultant surface brightness of the GRXE in this band is  $4.8 \times 10^{-11} \text{ erg cm}^{-2} \text{s}^{-1} \text{deg}^{-2}$ .

We have used the predictions from the previous section to estimate the contribution that ASBs, CVs and XRBs make to the GRXE. Fig. 11 shows the result in the form of the ‘resolved’ fraction (of the GRXE) plotted versus the threshold flux. As is evident, both from this figure and the source counts analysis (Fig. 9), the contribution of XRBs is negligible. Integrating down to an ultra-deep flux threshold of  $10^{-18} \text{ erg cm}^{-2} \text{s}^{-1}$ , the contribution of the



**Figure 11.** The fraction of the 2–10 keV GRXE that is resolvable into point sources. The GRXE is assumed to have a surface brightness of  $4.8 \times 10^{-11} \text{ erg cm}^{-2} \text{s}^{-1} \text{deg}^{-2}$ . The contribution of the different source types is integrated from a starting point at  $2 \times 10^{-13} \text{ erg cm}^{-2} \text{s}^{-1}$  (2–10 keV) down to faint fluxes. The curves correspond to the ASBs (red), the CVs (blue), the XRBs (green) and the total (i.e. combined) contribution (black).

ASBs is  $78 \pm 12$  per cent, with the CVs contributing a further  $16 \pm 4$  per cent. Clearly, a high fraction (and possibly the whole) of the 2–10 keV GRXE is resolved into sources.

A further consideration is whether the integrated emission of ASBs and CVs can explain the observed spectral form of the GRXE. We will discuss this issue in detail in the next section. However, in the meantime we have repeated the above analysis for a harder spectral range, namely the restricted 6–10 keV bandpass. Using the spectral forms previously defined for the two source populations, we find that the fraction of the 2–10 keV flux contained within this narrower band is 0.21 and 0.39 for the ASBs and CVs, respectively. Similarly, using the information in Ebisawa et al. (2008), we estimate the fraction of the 2–10 keV GRXE surface brightness residing in the 6–10 keV band to be 0.33. Applying these factors and assuming that the Galactic absorption in the 6–10 keV band is small, we find that the ASBs and CVs contribute  $62 \pm 10$  per cent and  $21 \pm 5$  per cent of the 6–10 keV GRXE. It follows that a very substantial fraction of GRXE can be attributed to low-luminosity sources even in the hard 6–10 keV band. We note, however, that this conclusion is (necessarily) very dependent on the spectral form assumed for the ASBs, namely that of an *apec* plasma with  $T = 35 \text{ MK}$  ( $kT = 3 \text{ keV}$ ) and  $Z = 0.4 Z_\odot$  (see §2.1). Repeating the above calculations for  $kT = 1.5 \text{ keV}$  and  $kT = 5 \text{ keV}$  changes the total ASB contribution to the 6–10 keV GRXE to  $13 \pm 2$  per cent in the case of the former, to  $90 \pm 13$  per cent for the latter. Thus, a factor 3 variation in the assumed temperature takes us from under-prediction to near over-prediction of the GRXE.

## 6 DISCUSSION

### 6.1 Composition of the Galactic source population

We have demonstrated that low-luminosity X-ray sources in the form of ASBs and CVs dominate the hard-band source counts recorded in the Galactic plane over a broad flux range. This is illustrated in Fig. 12 which shows the *predicted* make-up of the X-ray source population detected in surveys on the Galactic plane as a

<sup>6</sup> <http://cxc.cfa.harvard.edu/csc/>

function of the survey depth. A first point to note is that the contribution of extragalactic interlopers is at its largest at  $S_X \sim 10^{-14}$  erg cm $^{-2}$  s $^{-1}$ , which is close to the median source flux in the *Chandra* observations discussed earlier. The figure also illustrates how the composition of the Galactic population changes as the survey depth increases. Whilst the XRBs dominate at the bright end and the ASBs come to the fore at the faint end, the CVs make their highest contribution, namely  $\sim 40$  per cent of the total source number, at intermediate fluxes ( $S_X \sim 2 \times 10^{-13}$  erg cm $^{-2}$  s $^{-1}$ ). This latter point is consistent with recent results relating to the X-ray source population at these intermediate fluxes (Warwick et al. 2014).

Ebisawa et al. (2005) report the results from a NIR follow-up survey of their *Chandra* observations carried out at ESO using the NTT with the SofI NIR camera. This NIR survey was quoted as being complete down to  $\sim 18, 17$  and  $16$  mag in  $J, H$  and  $K_s$ , which is roughly 2 magnitudes fainter than 2MASS (Cutri et al. 2003; Skrutskie et al. 2006). The mosaic of NIR observations provided coverage of roughly two-thirds of the field-of-view encompassed by the *Chandra* observations. Using the results from Ebisawa et al. (2005) (their Table 1), we find that of the 77 sources comprising the hard-band *Chandra* sample considered earlier, 57 were within the sky region covered by the new NIR survey. Of these, 21 sources have plausible NIR counterparts, representing a 37 per cent identification rate. This is very comparable to the 0.32 fraction of X-ray detections predicted to be ASBs at  $S_X \approx 10^{-14}$  erg cm $^{-2}$  s $^{-1}$  (Fig. 12).

Of the 21 NIR counterparts, 16 have good photometry at  $J$  and  $K_s$  and hence can be located on a NIR colour-magnitude diagram (see Fig. 13). This figure also shows the tracks of several different types of stellar object in the colour-magnitude plane assuming that the visual absorption,  $A_V$ , in the Galactic plane increases at the rate of 2 mag kpc $^{-1}$  (equivalent to  $A_J = 0.56$  mag kpc $^{-1}$ ;  $A_K = 0.224$  mag kpc $^{-1}$ ). It is evident that the NIR parameters of the counterparts are consistent with those of stars. Interestingly 7 of these objects are aligned with the track for a K3 giant, suggesting that these may be RS CVn systems at the top-end of the XLF for the ASBs. Two further objects line-up with the track of a BOI supergiant and thus may be sources in which the hard X-ray emission is generated in shocked regions within an unstable wind or, in the case of massive binaries, in colliding winds (Mauerhan et al. 2010; Warwick et al. 2011). However, since the inferred 2–10 keV  $L_X$  is in excess of  $10^{32}$  erg s $^{-1}$ , the presence of an accreting high-mass system cannot be excluded (e.g. Anderson et al. 2011).

Fig. 13 also illustrates that CVs will, typically, be substantially fainter than the  $K_s = 16$  magnitude limit of the NIR survey. Similarly extragalactic sources are seen through a total hydrogen column density of at least  $6 \times 10^{22}$  cm $^{-2}$ , which equates to  $A_V = 33$  using the standard relation  $N_H/A_V = 1.8 \times 10^{21}$  cm $^{-2}$  mag $^{-1}$  (Predehl & Schmitt 1995) and corresponds to  $A_J \geq 9.2$  and  $A_K \geq 3.7$ . Hence the chances of identifying extragalactic sources in the NIR in these *Chandra* Galactic plane fields are remote. This substantiates the conclusion reached above that the hard-band selected *Chandra* sources with plausible NIR counterparts are predominantly ASBs.

## 6.2 The origin of the hard GRXE

In §5 we argued that ASBs and CVS produce the bulk of the GRXE. The fraction of the GRXE accounted for in our model amounted to  $94 \pm 14$  per cent in the full 2–10 keV band, falling to  $83 \pm 11$  per cent in the restricted 6–10 keV band. However, as demonstrated, these conclusions rely heavily on the validity of the spectral as-

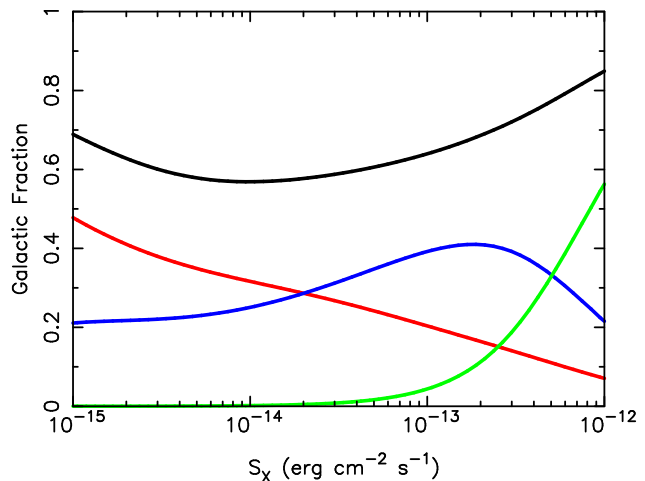


**Figure 12.** The predicted composition of the X-ray source population observed on the Galactic plane as a function of the limiting 2–10 keV flux. The various curves show the fraction of the population attributable to different source types: ASBs (red curve); CVs (blue curve); XRBs (green curve), all Galactic sources (black curve).

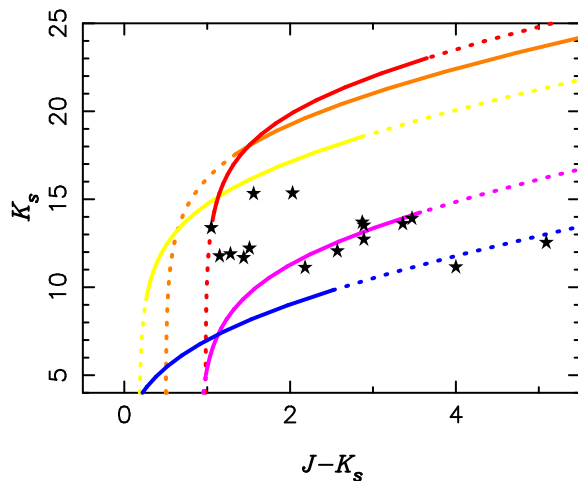


**Figure 13.** The  $K_s$  magnitude versus the  $J - K_s$  colour of the likely counterparts of 16 hard-band *Chandra* sources taken from the survey of Ebisawa et al. (2005) - shown as the black stars. The curves illustrate the tracks of different types of star as the distance is varied from 1 pc - 20 kpc, assuming that  $A_V$  in the Galactic plane increases at the rate of 2 mag kpc $^{-1}$ . *Brown curve*: a luminous CV with  $M_K = 5.0$  and intrinsic  $J - K_s = 0.5$ ; *Yellow curve*: a FOV dwarf star with  $M_K = 2.25$ ,  $J - K_s = 0.18$ ; *Red curve*: a M6V dwarf with  $M_K = 6.74$ ,  $J - K_s = 0.98$ ; *Purple curve*: a K3III giant with  $M_K = -2.03$ ,  $J - K_s = 0.90$ ; *Blue curve*: a BOI supergiant with  $M_K = -6.44$ ,  $J - K_s = -0.15$ . Apart from one exception, the curves become solid lines for stellar distances in the range 300 pc - 9 kpc, which roughly corresponds to an X-ray luminosity in the range  $10^{29-32}$  erg s $^{-1}$ , assuming an X-ray flux of  $10^{-14}$  erg cm $^{-2}$  s $^{-1}$  (2–10 keV). The exception is the curve for the CV where the distance limits were set at 3 and 16 kpc, corresponding to an X-ray luminosity in the range  $10^{31-32.2}$ . This figure is adapted from that shown in Warwick et al. (2014) (their Fig. 9).

sumptions underlying the calculations. Clearly, these assumptions need to be justified.

We first consider the X-ray spectra of CVs. In magnetic CVs, an accretion shock heats accreting material to high temperature ( $kT > 15$  keV). The resulting highly ionized plasma cools in the post-shock flow and eventually settles on to the white dwarf sur-

face via an accretion column. The resulting X-ray spectrum comprises a blend of components produced at a range of temperatures, densities and optical depths with a ‘characteristic’ temperature typically in the range 10–20 keV (e.g. Hellier, Mukai & Osborne 1998; Ezuka & Ishida 1999; Cropper et al. 1999; Yuasa et al. 2010).

Our (albeit small) sample of CVs is in fact comprised of both magnetic and non-magnetic systems in roughly equal measure. Non-magnetic CVs, which comprise the majority of the local CV population, are also well established sources of X-ray emission at the lower end of the range of X-ray luminosity exhibited by magnetic systems. In the current X-ray selected sample, the non-magnetic systems are, on average, roughly a factor 10 times less X-ray luminous than the confirmed magnetic systems. In most non-magnetic CVs the X-ray flux is produced as thermal emission from the boundary layer where the accretion flow slows down to match the rotation of the white dwarf surface (Patterson & Raymond 1985). The X-ray emission will again be comprised of a blend of components with temperatures ranging from the shock temperature at the outer edge of the boundary layer to the temperature of the white dwarf photosphere. Observationally, the characteristic temperature of the X-ray continuum emanating from non-magnetic CVs is typically in the range 5–20 keV. (Patterson & Raymond 1985; Baskill et al. 2005; Rana et al. 2006; Byckling et al. 2010; Reis et al. 2013).

In this paper we have modelled the X-ray spectra of the CVs (both magnetic and non-magnetic) as a 10-keV thermal bremsstrahlung continuum, which given the above, would seem to be representative of this class of object.

We next consider the X-ray spectra of the ASBs. In active stars the distribution of emission measure with temperature often shows a double peak, with the hotter component often extending up to 30–40 MK, if not higher (Güdel 2004). Stellar X-ray surveys have also shown that there is a relatively tight correlation between the characteristic coronal temperature (as determined from low resolution spectral data) of the ‘hotter’ component and the normalized coronal luminosity  $L_X/L_{\text{bol}}$  (e.g. Güdel et al. 1997; Schmitt 1997). This correlation also appears to extend into the regime of stellar flares, in the sense that the larger flares are generally hotter (e.g. Telleschi et al. 2005; Aschwanden et al. 2008). Large flares have durations typically ranging from hours to days with total X-ray luminosities and temperatures reaching up to  $10^{33}$  erg s $^{-1}$  and 100 MK, respectively (e.g. Pan et al. 1997; Tsuboi et al. 1998; Favata & Schmitt 1999; Pandey & Singh 2008; Pandey & Singh 2012). Clearly the occurrence of giant flares in very active systems, for example RS CVn binaries, will enhance the detection rate of such sources in hard-band selected X-ray samples (e.g. Pye & McHardy 1983; Matsuoka et al. 2012). The fraction of the time that active systems spend in a flaring state is also relatively high. For example, Pandey & Singh (2012) quote a flare-occurrence rate of  $\sim 20$  per cent for RS CVn binaries, whereas Pandey & Singh (2008) obtain a similar rate for flares on G-K dwarf stars. Finally, we note that recent high-resolution X-ray grating spectroscopy has revealed that highly-active stars show the presence of an inverse ‘First Ionization Potential’ effect, namely stellar spectra with depleted abundances of elements such as Mg and Fe relative to solar photospheric values (see Güdel 2004 - Fig 37).

Given the above properties of stellar coronae, our assumed spectral model for the ASBs, namely a  $T = 35$  MK ( $kT = 3$  keV) *apex* plasma with a metal abundance  $Z = 0.4 Z_{\odot}$ , would again seem to be representative of this object class.

Although we have demonstrated that the integrated emission

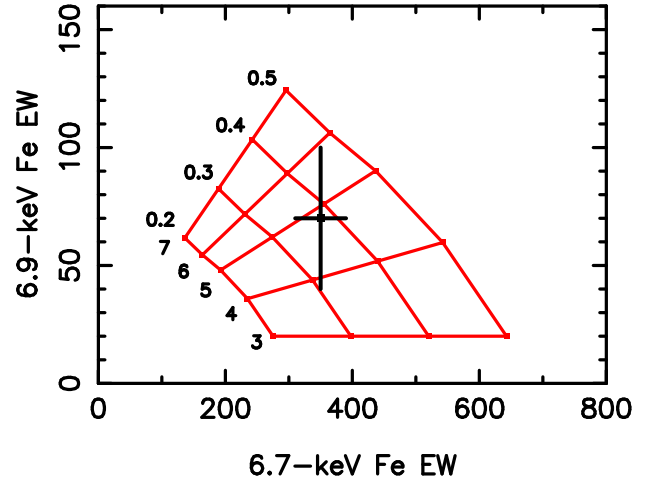


**Figure 14.** The EW of the 6.9-keV H-like Fe K $\alpha$  line plotted versus the EW of the 6.7-keV He-like Fe K $\alpha$  line. The measurement (black point plus error bars) is from Suzaku (Ebisawa et al. 2008). The grid (red lines) indicates the EWs expected for a 3:1 mix of ASB and CV spectra on the basis of different assumptions for the ASB spectra. The grid points correspond to coronal plasma temperatures ranging from 3 to 7 keV in 1 keV steps with iron abundances ranging from 0.2 to 0.5  $Z_{\odot}$  in 0.1  $Z_{\odot}$  steps (as labelled).

of unresolved ASBs and CVs may well produce the bulk of the GRXE intensity in both the broad 2–10 keV band and the more restricted 6–10 keV range, a further consideration is whether a mix of ASB and CV spectra can explain the observed Fe-line features in the GRXE spectrum. Ebisawa et al. (2008) measure emission-line equivalent widths (EWs) for the He-like Fe K $\alpha$  line at 6.67 keV and the H-like Fe K $\alpha$  line at 6.96 keV of  $350 \pm 40$  eV and  $70 \pm 30$  eV, respectively. An Fe-K fluorescent line arising in neutral atoms or lightly ionized ions was also observed near 6.4 keV with an EW of  $80 \pm 20$  eV.

For CVs, the line equivalent widths are found to be, typically,  $\sim 170$  eV for the 6.7-keV line and  $\sim 100$  eV for the two other Fe lines, although with a very considerable source-to-source scatter (Ezuka & Ishida 1999; Hellier, Mukai & Osborne 1998; Hellier & Mukai 2004; Bernardini et al. 2012; Warwick et al. 2014). In the case of the ASBs, the assumed 3-keV spectral model, implies a He-like 6.7-keV Fe-K $\alpha$  line with 800 eV EW. However at this plasma temperature, there is negligible H-like 6.9-keV Fe-line photon flux. In order to enhance the H-like line, the temperature needs to rise by roughly a factor of two; for example for a  $Z = 0.4 Z_{\odot}$  plasma with  $kT$  in the range 5–7 keV, the EW of the 6.9-keV Fe-line line is between 90–140 eV. The impact of such a temperature enhancement is illustrated in Fig. 14, which shows the 6.7-keV and 6.9-keV Fe line EWs expected for a 3:1 mix of ASB and CV components, as the temperature characterizing the ASB spectrum varies from 3 keV up to 7 keV. It would seem entirely plausible that the ASBs present in our XSS sample are in flare states characterized by this range of temperature.

Although a suitable blend of hard X-ray emission from flaring ASBs together with a more modest contribution from CVs has the potential to account for the He-like and H-like Fe-K lines observed in the GRXE spectrum, the origin of the Fe-K fluorescent line is more problematic. The 6.4-keV Fe fluorescent line is very often too faint to be detected in the spectra of ASBs (Güdel & Nazé 1997), although some exceptions have been reported. For example, a strong 6.4-keV line has been observed in several protostars where the fluorescence is attributed to the irradiation of the circumstellar



disk by X-rays generated in hot coronal loops (e.g. Imanishi et al. 2001; Tsujimoto et al. 2005; Skinner et al. 2007). There are also a limited number of reports of the detection of 6.4-keV emission in more evolved stars, where the fluorescence could originate in the photosphere. For example, Osten et al. (2007) measured a prominent 6.4-keV Fe line in the spectrum of the RS CVn binary II Peg during a superflare, with an EW ranging from 20 - 60 eV. More recently, Testa et al. (2008) found evidence for photospheric fluorescence in the single G-type star HR 9024 with a 6.4-keV line of EW comparable to the top end value measured for II Peg. However, notwithstanding these isolated observations, the hypothesis that stellar flares might give rise to the fluorescent emission present in the GRXE spectrum (arising from Fe and other elements) remains unsubstantiated.

The 6.4-keV emission may in fact originate in an entirely different way, namely in the scattering of the radiation of bright XRBs by the interstellar medium. In a recent paper Molaro et al. (2014) argue that between 10-30 per cent of the broad-band GRXE flux might originate in this way. The results presented in this paper do not exclude this possibility, particularly if the contribution from scattering in our fiducial direction ( $l = 28.5^\circ$ ) is at the lower-end of the quoted range. The scattered flux will be imprinted with a fluorescent Fe line of high equivalent width ( $\sim 1$  keV) for a scattering medium with a near-solar Fe abundance (Sunyaev & Churazov 1998). It follows that even a modest  $\sim 10$  per cent contribution from scattered X-rays to the continuum at 6 keV might explain the observed EW of the 6.4-keV line feature seen in the GRXE spectrum.

A further characteristic of the GRXE that merits consideration is the observed fluctuation in its intensity on a scale of a few degrees. For example, in the plot of the GRXE surface brightness (4–10 keV) versus Galactic longitude presented by Sugizaki et al. (2001) (their Fig. 2), peak-to-peak variations of up to 20 per cent are evident on this angular scale (measured with respect to a smoothly varying Galactic profile). This effect cannot be explained in terms of statistical fluctuations in the number of sources along the line of sight (within the context of our Galactic-scale source distribution model), since the source number density at which a sizeable fraction of the GRXE intensity is produced is too high. It is more likely that these GRXE intensity variations coincide with specific Galactic plane features such as molecular-cloud complexes, OB associations and star-formation regions. In this context our modelling of the Galactic source population is most certainly incomplete, in that it excludes the likely contribution to the GRXE of young stellar objects (e.g. Feigelson & Montmerle 1999; Imanishi et al. 2003; Güdel 2004) and massive stars (e.g. Mauerhan et al. 2010; Anderson et al. 2011; Anderson et al. 2014), neither of which were represented in the high-latitude XSS survey which provides the basis of our study.

The picture which emerges is that ASBs and CVs likely give rise to the bulk of the smoothly-varying GRXE (say nominally  $\sim 80$  per cent of its typical intensity), with a rough 3:1 split between the ASBs and CV contributions. Superimposed on this, at the level of 10 percent or more, is the diffuse scattered X-ray emission from bright XRBs, which carries the imprint of the 6.4 keV fluorescent line. As a tracer of dense molecular gas and HI clouds, this component is predicted to have a clumpy distribution (Molaro et al. 2014). Finally, a further modest contribution (perhaps  $\sim 10$  per cent) may be contributed by other relatively young Galactic source populations, which show a narrow concentration on the plane in specific Galactic complexes and features. Clearly the challenge for the future is to apply fully quantitative tests of this description.

## 7 SUMMARY AND CONCLUSIONS

Using the XSS catalogue, we construct a sample of low-luminosity Galactic X-ray sources. This hard-band selected sample splits into two subsets, namely 46 objects identified as coronally-active single stars and binaries (the ASBs) and a further 16 sources which are likely CVs. We use published distances and/or our own distance estimates to determine the distribution of X-ray luminosity within each source class. For the ASBs the 2–10 keV X-ray luminosities span the range  $10^{28-32.5}$  erg s $^{-1}$ , whereas for the CVs, which include both magnetic and non-magnetic systems in roughly equal numbers, the range is  $10^{30.5-33.5}$  erg s $^{-1}$ .

We go on to determine the 2–10 keV X-ray Luminosity Function (XLF) for each population and find that the XLF of the ASBs has a normalization roughly a factor 2 higher than previous estimates and extends at least a decade lower in X-ray luminosity than previously projected. The 2-10 keV X-ray emissivity of the ASBs and CVs, scaled to the local stellar mass density, is found to be  $1.08 \pm 0.16 \times 10^{28}$  and  $2.5 \pm 0.6 \times 10^{27}$  erg s $^{-1}$  M $_{\odot}^{-1}$  respectively. The implied total X-ray emissivity is at least a factor 2 higher than previously reported.

We use the new XLFs to predict the 2–10 keV X-ray source counts on the Galactic plane in the direction  $l = 28.5^\circ$ , a region for which a number of useful observational datasets are available. The predicted source counts are in good agreement with the available observational constraints. As the flux threshold is reduced from  $10^{-12}$  erg cm $^{-2}$  s $^{-1}$  down to  $10^{-15}$  erg cm $^{-2}$  s $^{-1}$ , XRBs, CVs, extragalactic sources and finally ASBs, each in turn, make the largest contribution to the source number counts.

We also estimate the total X-ray surface brightness attributable to the ASB and CVs source populations integrated along the line of sight through the Galactic disc. We find that bulk the GRXE signal ( $\sim 80$  per cent in the restricted 6-10 keV band) can be attributed to the X-ray emission of these two populations, with a rough 3:1 split between the ASBs and CV contributions. The predicted number density of these sources is such that their integrated signal (after suitably excluding the brightest sources) should be a smoothly varying function of Galactic longitude (and latitude). Superimposed on this will be the scattered X-ray emission from bright Galactic XRBs together with a (modest) contribution from relatively young Galactic source populations. Together these components might typical contribute  $\sim 20$  per cent of the total GRXE flux but with a clumpy distribution tracing Galactic plane features and complexes.

Much of the hard X-ray emission attributed to the ASBs is likely to be produced during energetic flare states. Furthermore, it is reasonable to suppose that the hard-band selection preferentially captures ASBs in such flaring episodes. It seems plausible that the characteristic temperature of the coronal loops which generate these flares will span the range 3-7 keV and thereby generate the bulk of the He-like and H-like Fe-K $\alpha$  emission seen in the GRXE spectrum. However, the 6.4-keV Fe fluorescent line seen in the GRXE spectrum is more likely to originate in the diffuse scattered component referred to above.

## ACKNOWLEDGEMENTS

This paper is based on data from the *XMM-Newton* slew survey. In carrying out this research, extensive use has been made of ALADIN, VizieR and SIMBAD at the CDS, Strasbourg, France. Similarly, the facilities provided by the Chandra X-ray Center as part of the Chandra Data Archive proved very valuable.

## REFERENCES

- Ak, T., Bilir, S., Ak, S., Eker Z., 2008, *New Ast.*, 13, 133
- Anderson G.E. et al., 2011, *ApJ*, 727, 105
- Anderson G.E. et al., 2014, *ApJS*, 212, 13
- Aschwanden, M.J., Stern R.A., Güdel, M., 2008, *ApJ*, 672, 659
- Baskill D. S., Wheatley P. J., Osborne J. P., 2005, *MNRAS*, 357, 626
- Bauer F.E., Alexander D.M., Brandt W.N., Schneider D.P., Treister E., Hornschemeier A.E., Garmire G.P., 2004, *AJ*, 128, 2048
- Bernardini F., de Martino D., Falanga M., Mukai K., Matt G., Bonnet-Bidaud J.-M., Masetti N., Mouchet M., 2012, *A&A*, 542, A22
- Beuermann K., Harrison Th. E., McArthur B. E., Benedict G.F., Gänsicke B. T., 2004 *A&A*, 419, 291
- Buckley D.A.H., Tuohy I.R., *ApJ*, 344, 376
- Byckling K., Mukai K., Thorstensen J. R., Osborne J. P., 2010, *MNRAS*, 408, 2298
- Carpenter J.M., 2001, *AJ*, 121, 2851
- Carpenter J.M., Mamajek E.E., Hillenbrand L.A., Meyer M.R., 2009, *ApJ*, 705, 1646
- Cropper M., Wu K., Ramsay G., Kocabiyik A., 1999, *MNRAS*, 306, 684
- Cutri, R. M., et al., 2003, Explanatory Supplement to the 2MASS All Sky Data Release and Extended Mission Products (Pasadena:IPAC/Caltech)
- de Zeeuw P. T., Hoogerwerf R., de Bruijne J. H. L., Brown A. G. A., Blaauw A. 1999, *AJ*, 117, 354
- Ebisawa K., Maeda, Y., Kanade H., Yamauchi, S., 2001, *Science*, 293, 1633
- Ebisawa K. et al., 2005, *ApJ*, 635, 214
- Ebisawa K., Yamauchi S., Tanaka Y., Koyama K., Ezoe Y., Bamba A., Kokubun M., Hyodo Y., Tsujimoto M., Takahashi H., 2008, *PASJ*, 60, S223
- Ezuka H., Ishida M., 1999, *ApJS*, 120, 277
- Favata F., Schmitt J.H.M.M., *A&A*, 350, 900
- Feigelson E.D., Montmerle T., 1999, *ARA&A*, 37, 363
- Forman W., Jones C., Julien P., Murray S., Peters G., Tananbaum H., Giacconi R., 1978, *ApJS*, 38, 357
- Gänsicke, B.T., Koester D., 1999, *A&A*, 346, 151
- Güdel, M., 2004, *Astron Astrophys Rev*, 12, 71
- Güdel, M., Guinan S.L., Skinner S.L., 1997, *ApJ*, 483, 947
- Güdel, M., Nazé, Y., 2009, *A&ARv*, 17, 309
- Hands A. D. P., Warwick R. S., Watson M. G., Helfand D. J., 2004, *MNRAS*, 351, 31
- Heard V., Warwick R. S., 2013, *MNRAS*, 428, 3462
- Hellier C., Mukai K., Osborne J. P., 1998, *MNRAS*, 297, 526
- Hellier C., Mukai K., 2004, *MNRAS*, 352, 1037
- Hoard D.W., Linnell A.P., Szkody P., Fried R.E., Sion E.M., Hubeny I., Wolfe M.A., 2004, *ApJ*, 604, 346
- Hong J., 2012, *MNRAS*, 427, 1633
- Imanishi K., Koyama K., Tsuboi, Y., 2001, *ApJ*, 557, 747
- Imanishi K., Nakajima M., Tsujimoto K., Koyama K., Tsuboi, Y., 2003, *PASJ*, 55, 653
- Kaneda H., Makishima K., Yamauchi S., Koyama K., Matsuzaki K., Yamasaki N. Y., 1997, *ApJ*, 491, 638
- Kiraga, M., 2012, *Acta Astron*, 62, 67
- Koyama K., Makishima K., Tanaka Y., Tsunemi H., 1986a, *PASJ*, 38, 121
- Koyama K., Ikeuchi S., Tomisaka K., 1986b, *PASJ*, 38, 503
- Koyama K., Maeda, Y., Sonobe T., Takeshima T., Tanaka Y., Yamauchi, S., 1996, *PASJ*, 48, 249
- Koyama K. et al., 2007, *PASJ*, 59, 245
- Krivonos R., Revnivtsev M., Churazov E., Sazonov S., Grebenev S., Sunyaev R., 2007, *A&A*, 463, 957
- Lepine S., Gaidos E., 2011, *AJ*, 142, 138
- Matsuoka M. et al., 2012, *AIPC*, 1427, 294
- Mauerhan J. C., Muno M. P., Morris M. R., Stolovy S. R., Cotera A., 2010, *ApJ*, 710, 706
- McHardy, I. M., Lawrence, A., Pye, J. P., Pounds, K. A., 1981, *MNRAS*, 197, 893
- Molaro M., Khatri R., Sunyaev R.A., 2014, *A&A*, 564, A107
- Moretti A., Campana S., Lazzati D., Tagliaferri G., 2003, *ApJ*, 588, 696
- Morihana K., Tsujimoto, M., Yoshida T., Ebisawa K., 2013, *ApJ*, 766, 14
- Muno M.P., Baganoff F.K., Bautz M.W., Brandt W.N., Broos P.S., Feigelson E.D., Garmire G.P., Morris M.R., Ricker G.R., Townsley L.K., 2003, *ApJ*, 589, 225
- Muno, M.P. et al., 2004, *ApJ*, 613, 1179
- Muno, M.P., Bauer F.E., Bandyopadhyay R.M., Wang Q.D., 2006, *ApJS*, 165, 171
- Nebot Gómez-Morán, A. et al., 2013, *A&A*, 553A, 12N
- Nishiyama S. et al., 2013, *ApJL*, 769, L28
- Norton A.J., Beardmore A.P., Retter A., Buckley D.A.H., 2000, *MNRAS*, 312, 362
- Osten, R.A., Drake, S., Tueller J., Cummings J., Perri M., Moretti A., Covino S., *ApJ*, 654, 1052
- Pan H.C., Jordan C., Makishima K., Stern R.A., Hayashida K., Inda-Koide M., *MNRAS*, 285, 735
- Pandey J.C., Singh K.P., *MNRAS*, 387, 1627
- Pandey J.C., Singh K.P., *MNRAS*, 419, 1219
- Parisi P., 2012, *A&A*, 545, A101
- Patterson J., Raymond J.C., 1985, *ApJ*, 292, 535
- Perryman M. A. C., Lindegren L., Kovalevsky J., et al., 1997, *A&A*, 323, L49
- Piccinotti G., Mushotzky R. F., Boldt E. A., Holt S. S., Marshall F. E., Serlemitsos P. J., Shafer R. A., 1982, *ApJ*, 253, 485
- Pickles A.J., 1998, *PASP*, 110, 863
- Predehl P., Schmitt J., 1995, *A&A*, 293, 889
- Pretorius M.L., Knigge, C., 2012, *MNRAS*, 419, 1442
- Pretorius M.L., Knigge, C., Schwobe A.D., 2013, *MNRAS*, 432, 570
- Pye J.P., McHardy I.M., 1983, *MNRAS*, 205, 875
- Rana V.R., Singh K. P., Schegel E. M., Barrett P. E., 2006, *ApJ*, 1042
- Reis R. C., Wheatley P. J., Gänsicke, B. T., Osborne J. P., 2013, *MNRAS*, 430, 1994
- Revnivtsev M., Sazonov S., Gilfanov M., Churazov E., Sunyaev R., 2006, *A&A*, 452, 169
- Revnivtsev M., Sazonov S., 2007, *A&A*, 471, 159
- Revnivtsev M., Sazonov S., Krivonos R., Ritter H., Sunyaev R., 2008, *A&A*, 489, 1121
- Revnivtsev M., Sazonov S., Churazov E., Forman W., Vikhlinin A., Sunyaev R., 2009, *Nature*, 458, 1142
- Revnivtsev M., Sazonov S., Forman W., Churazov E., Sunyaev R., 2011, *MNRAS*, 414, 495
- Revnivtsev M., Molokov S.V., 2012, *MNRAS*, 424, 2330
- Riaz B., Gizis J.E., Harvin J., 2006, *AJ*, 132, 866
- Roeser S., Demleitner M., Schilbach E., 2010, *AJ*, 139, 2440
- Saxton R.D., Read A.M., Esquej M.P., Freyberg M.J., Altieri, B., Bermejo, D., 2008, *A&A*, 480, 611
- Sazonov S., Revnivtsev M., Gilfanov M., Churazov E., Sunyaev R., 2006, *A&A*, 450, 117

- Schmidt M., 1968, *ApJ*, 151, 393
- Schmitt J.H.M.M., 1997, *A&A*, 318, 215
- Skinner S.L., Simmons A.E., Audard M., Güdel M., 2007, *ApJ*, 658, 1144
- Skrutskie, M. F. et al., 2006, *AJ*, 131, 1163
- Strong A.W., Diehl R., Halloin H., Schnfelder V., Bouchet L., Mandrou P., Lebrun F., Terrier R., 2005, *A&A* 444, 495
- Sugizaki M., Mitsuda K., Kaneda H., Matsuzaki K., Yamauchi S., Koyama K., 2001, *ApJS*, 134, 77
- Sunyaev R., Churazov E., 1998, *MNRAS*, 297, 1279
- Tanaka, Y., 2002, *A&A*, 382, 1052
- Tanaka, Y., Yamauchi, S., 2010, in Makishima K., ed., *The Energetic Cosmos: from Suzaku to ASTRO-H*, Proceedings of the 3rd Suzaku Conference, 2009, Otaru, Japan. JAXA Special Publication JAXA-SP-09-008E.
- Telleschi A., Güdel M., Briggs K., Audard M., Ness, J-U., Skinner S.L., 2005, *ApJ*, 625, 653
- Testa P. Drake J.J., Ercolano B., Reale F., Huenemoerder D.P., Affer L., Micela G., Garcia-Alvarez D., 2008, *ApJ*, 675, 97
- Thorstensen J.R., 2003, *AJ*, 126, 3017
- Thorstensen J.R., Lepine S., Shara M., 2006, *PASP*, 118, 1238
- Tinney C.G., Reid I.N., Mould J.R., 1993, *ApJ*, 414, 254
- Tsuboi Y., Koyama K., Murakami H., Hayashi M., Skinner S., Ueno S., 1998, *ApJ*, 503, 894
- Tsujimoto M., et al. *ApJS*, 160, 503
- Uchiyama, H., Nobukawa, M., Tsuru, T. G., Koyama, K., Matsumoto, H., 2011, *PASJ*, 63, 903
- Uchiyama, H., Nobukawa, M., Tsuru, T. G., Koyama, K., 2013, *PASJ*, 65, 19
- Valinia A., Marshall F. E., 1998, *ApJ*, 505, 134
- Valinia A., Tatischeff V., Arnaud K., Ebisawa K., Ramaty R., 2000, *ApJ*, 543, 733
- van Leeuwen F., 2007a *Hipparcos*, the new reduction of the raw data (Dordrecht:Springer)
- van Leeuwen F., 2007b, *A&A*, 474, 653
- Warwick R. S., Marshall N., Fraser G. W., Watson M. G., Lawrence A., Page C. G., Pounds K. A., Ricketts M. J., Sims M. R., Smith A., 1981, *MNRAS*, 197, 865
- Warwick R. S., Turner M. J. L., Watson M. G., Willingale R., 1985, *Nature*, 317, 218
- Warwick R. S., Pérez-Ramírez D., Byckling K., 2011, *MNRAS*, 413, 595
- Warwick R. S., Saxton R.D., Read A.M., 2012, *A&A*, 548, A99
- Warwick R. S., Byckling K., Pérez-Ramírez D., 2014, *MNRAS*, 438, 2967
- Wood K. S., Meekins J. F., Yentis D. J., Smathers H. W., McNutt D. P., Bleach R. D., Friedman H., Byram E. T., Chubb T. A., Meidav M., 1984, *ApJS*, 56, 507
- Worrall D. M., Marshall F. E., Boldt E. A., Swank J. H., 1982, *ApJ*, 255, 111
- Yamasaki N. Y. et al., 1997, *ApJ*, 481, 821
- Yamauchi S., Koyama K., 1993, *ApJ*, 404, 620
- Yamauchi S., Kaneda H., Koyama K., Makishima K., Matsuzaki K., Sonobe T., Tanaka Y., Yamasaki N., 1996, *PASJ*, 48, L15
- Yamauchi S., Ebisawa K., Tanaka Y., Koyama K., Matsumoto H., Yamasaki N. Y., Takahashi H., Ezoe Y., 2009, *PASJ*, 61, S225
- Yuasa T., Nakazawa K., Makishima K., Saitou K., Ishida M., Ebisawa K., Mori H., Yamada S., 2010, *A&A*, 520, A25
- Yuasa T., Makishima K., Nakazawa K., 2012, *ApJ*, 753, 129